A chemical approach to raise cell voltage and suppress phase transition in O3 sodium layered oxide electrodes

WILEY-VCH

DOI: 10.1002/ aenm.201702599
Article type: Full paper

A CHEMICAL APPROACH TO RAISE CELL VOLTAGE AND SUPPRESS PHASE TRANSITION IN O3 SODIUM LAYERED OXIDE ELECTRODES.

*Mariyappan Sathiya,[†] Quentin Jacquet,[†] Marie-Liesse Doublet, Olesia M. Karakulina, Joke Hadermann and Jean-Marie Tarascon.**

Dr. M. S, Q. J and Prof. J-M. T
Collège de France, 11, Place Marcelin Berthelot, 75231 Paris, France
E-mail: jean-marie.tarascon@college-de-france.fr
Q. J and Prof. J-M. T
Réseau sur le Stockage Electrochimique de l'Energie (RS2E), FR CNRS 3459, France
Sorbonne Universités - UPMC Univ. Paris 06, 4 place Jussieu, F-75005 Paris, France
Dr. M-L. D
Institut Charles Gerhardt, CNRS UMR5253, Université Montpellier, 34 095 Montpellier, France
O. M. K and Dr. J. H
EMAT, University of Antwerp, Groenenborgerlaan 171, B-2020, Antwerp, Belgium

Keywords: Sodium ion battery, O3-type layered oxide, phase transition, charge localization, redox potential

Sodium ion batteries (NIBs) are one of the versatile technologies for low cost rechargeable batteries. O3-type layered sodium transition metal oxides ($NaMO_2$, M = transition metal ions) are one of the most promising positive electrode materials, capacity-wise. However, the use of O3 phases is limited due to their low redox voltage and associated multiple phase transitions which are detrimental for long cycling. Herein, we proposed a simple strategy to successfully combat these issues. It consists in the introduction of a larger, non-transition metal ion Sn^{4+} in $NaMO_2$ to prepare a series of $NaNi_{0.5}Mn_{0.5-y}Sn_yO_2$ (y=0- 0.5) compositions with attractive electrochemical performances, namely for y=0.5, which shows a single phase transition from O3 ⇔ P3 at the very end of the oxidation process. Na-ion $NaNi_{0.5}Sn_{0.5}O_2$/C coin cells are shown to deliver an average cell voltage of 3.1 V with an excellent capacity retention as compared to an average step-wise voltage of ~2.8 V and limited capacity retention for the pure $NaNi_{0.5}Mn_{0.5}O_2$ phase. This study potentially shows the way to manipulate the O3 $NaMO_2$ for facilitating their practical use in NIBs.

1. Introduction

Electrochemical energy storage devices have become indispensable part of life and introduction of light weight Li-ion batteries made it easier to store and restore electrical power wherever it is needed. The major advantage of Li-ion batteries relies on their large energy density and excellent cycling/calendar life. However, owing to the foreseen EV market demand for longer autonomy, the research towards higher energy density electrode materials is being intensively pursued.[1] In contrast, cost rather than energy density is the overriding factor regarding large storage systems for grid applications.[2] In this regard, sodium ion batteries stand as serious contenders.[3] However, most of the sodium ion electrodes show both reduced capacity and redox voltage with respect to their lithium counter parts.[4] Thus, advanced electrode materials with greater specific capacity, higher cell voltage, better rate capability and long cycle life while being low cost and non-toxic are sorely needed.[5]

O3-type layered sodium transition metal oxides derived from their lithium based homologues $LiCoO_2$, $LiNi_{1-x-y}Mn_xCo_yO_2$, $LiNi_{1-x-y}Co_xAl_yO_2$ etc., are being widely studied as positive electrode material for Na-ion batteries.[6] Sodium-based O3-type layered oxides having a high reversible capacity were reported with a wide variety of transition metal ions.[7, 8, 9] However, these materials show numerous phase transitions during sodium de-insertion/ insertion (charge/ discharge) resulting in poor capacity retention on long-term cycling. The major phase transition associated with these materials is the transition from O3 to P3 [9, 10] with the corresponding structures shown in supplementary information Figure S1.

In the Na_xMO_2 phase stability diagram ($0 \leq x \leq 1$, M= transition metal ion(s)), the O3 structure with Na in octahedral positions are usually preferred because they minimize the O-O interlayer repulsions.[11] This contrasts with the P3 phase in which the sodium coordination polyhedral shares face with the MO_6 octahedral so that the oxygen lies on top of each other (figure S1). For this reason, the P3 phase is relatively less stable than the O3 phase. However,

for certain values of x in Na_xMO_2, the O3 ⇔ P3 phase transition is triggered by Na-vacancy ordering in order to reduce Na-Na repulsion.[12, 13] This happens via a simple gliding of the MO_2 layer without breaking/ making of M-O bonds,[11] which when repeated upon subsequent charges/discharges is detrimental to the cell performance, hence leading to severe capacity decay during cycling. Moreover, the hexagonal O3 ⇔ monoclinic O'3 ⇔ hexagonal P3 transition occurs at a low voltage (< 3 V vs. Na^+/ Na^0 and ~ 2.5 V vs. Hard carbon) in most of the O3 $NaMO_2$ materials reported so far.[8] Application-wise, this is quite penalizing in terms of energy density as almost 40-50% of the total capacity lies in the low voltage region.

To circumvent these issues inherent to the O3 $NaMO_2$ materials, a specific design strategy is needed. Herein we present a strategy relying on chemical substitution and consisting in the making of O3-type $NaMM'O_2$ phases where M and M' are redox active and inactive metal ions, respectively. We centered our interest towards the previously reported O3 $NaNi_{0.5}Mn_{0.5}O_2$ phase[10, 14] and envisioned to replace, Mn^{4+} by a non-transition metal ion such as Sn^{4+} which is larger than Mn^{4+} (0.69 Å vs. 0.53 Å). Besides size, our choice for Sn^{4+} is also nested in its inability to interact with oxygen through its *d* orbitals, hence reducing orbital overlap and favoring charge localization in the metallic layer. This effect, combined with the concomitant increase of bond ionicity should be beneficial to increase the redox potential as well documented.[15] Secondly, increasing the ionic nature of the crystal lattice is expected to destabilize the P3 phase which deviates from the Pauling's third rule by sharing faces between NaO_6 and MO_6 polyhedra.[11, 16] The destabilization of P3 phase, could therefore suppress the phase transition from O3 to P3.

Thus, a series of $NaNi_{0.5}Mn_{0.5-y}Sn_yO_2$ phases with y = 0-0.5 were prepared and analyzed for their structural and electrochemical properties through experimental and computational techniques. The $NaNi_{0.5}Sn_{0.5}O_2$ composition is shown to display an average cell voltage of 3.1 V vs. Hard carbon with a single phase transition and better performances than its $NaNi_{0.5}Mn_{0.5}O_2$ counterpart in terms of energy density, long-term cycling and rate capability.

2. Results and discussion

All $NaNi_{0.5}Mn_{0.5-y}Sn_yO_2$ (y = 0-0.5) materials were prepared by classical solid state synthesis using a slight excess of Na/Ni (5%) ratio to avoid/reduce the formation of NiO impurities in the material. The collected X-ray powder diffraction (XRD) patterns shown in **Figure 1** confirm the existence of O3-$NaNi_{0.5}Mn_{0.5}O_2$ phase (y=0). The progressive substitution of Mn by Sn initially results in a broadening of the Bragg peaks for y=0.1 and 0.2 suggesting a bi-phasic domain further confirmed by the successful fitting of the patterns by two phases having close lattice parameters. These broad peaks were found to sharpen and shift towards lower angles with increasing the Sn content, indicative of a solid solution for compositions ranging from y = 0.3 to 0.5 with a gradual volume increase expected by the substitution of smaller Mn^{4+} (0.53 Å) by larger Sn^{4+} (0.69 Å) (Vegard's law). Worth mentioning is that, independent of the synthesis parameters tried (various annealing times, temperatures and cooling rates) we could not obtain the y=0.1 and 0.2 samples as single phase. Moreover, interesting to note is the presence of NiO impurities mainly in the y=0, 0.1 and 0.2 that could never be eliminated independently of the excess of Na_2CO_3 used, suggesting a lower solubility of Mn and Ni in comparison to Sn and Ni due to the size difference between Ni^{2+} (0.69 Å) and Mn^{4+} (0.53 Å) ions.

The XRD patterns of $NaNi_{0.5}Mn_{0.5-y}Sn_yO_2$ (y = 0, 0.3-0.5) were refined using hexagonal cell typical to that of O3 $NaMO_2$ phase (supporting information Figure S2(a) and the table ST1) in the *R* -3*m* space group. The obtained lattice parameters are plotted in inset of Figure 1 where both *a* and *c* show a monotonous increase with increasing the amount of Sn^{4+} in the structure. The increase in the *a* lattice indicates an equal increase in the Na-Na distance and hence the reduction of Na-Na intra layer repulsions with Sn substitution. Equally, we find over the same composition range, an increase in the O-O interlayer distances from 3.646 Å ($NaNi_{0.5}Mn_{0.5}O_2$) to 3.658 Å ($NaNi_{0.5}Sn_{0.5}O_2$) as calculated from the refined structures. Such Sn-driven lengthening of the O-O distances could help in reducing the O-O interlayer repulsions and

improves the phase stability over a wide range of sodium stoichiometry, provided that the oxygen charge increases in a lesser extent than the M-O bond lengths.

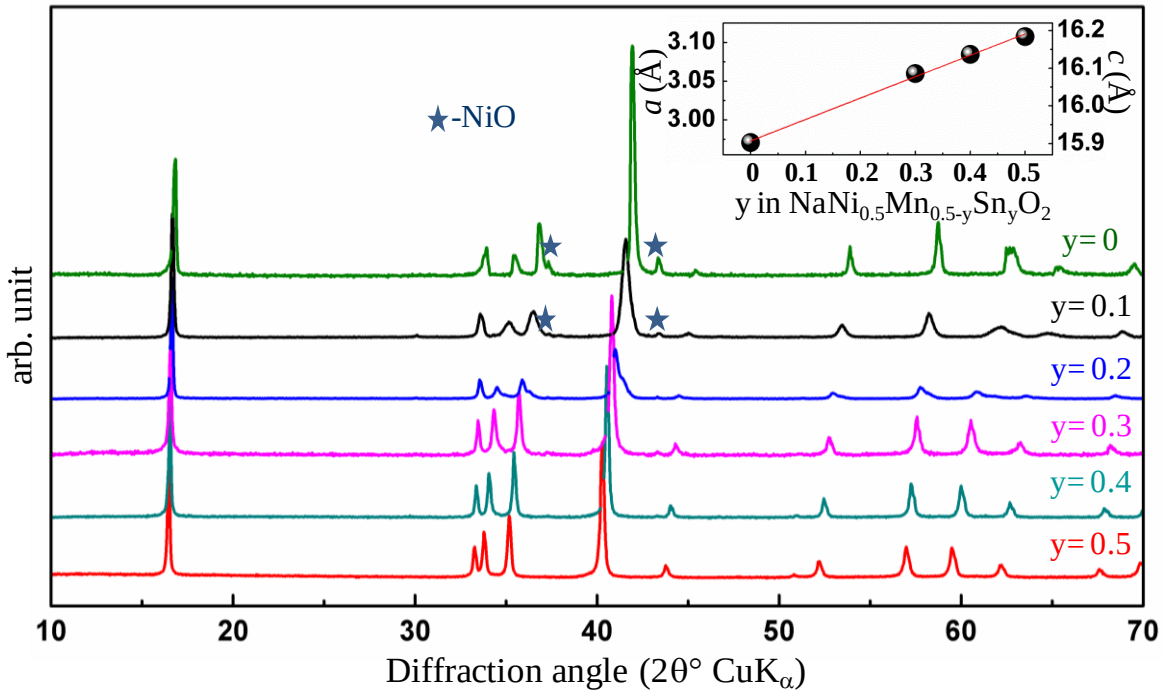

Figure 1: Powder XRD pattern of the $NaNi_{0.5}Mn_{0.5-y}Sn_yO_2$ compounds prepared by solid state synthesis with the inset showing the change in lattice parameter. The lattice parameter values are derived by refining the XRD pattern within the *R* -3*m* space group in hexagonal lattice.

To check for a possible presence of Ni/Sn ordering within the metal layers in $NaNi_{0.5}Sn_{0.5}O_2$ we performed Transmission Electron Microscopic (TEM) analysis. Electron diffraction in **Figure 2** (a,b) shows that the crystal structure corresponds to *R* -3*m* similar to that of $LiCoO_2$. The cell parameters are a= 3.1 Å, c= 16.1 Å and γ= 120° which is in agreement with the XRD results. Rows of diffuse intensity at 1/3(1 -2 *l*) and 2/3(1 -2 *l*) on the [210] pattern are characteristically caused by the occurrence of stacking faults. No sharp superstructure reflections are present in the electron diffraction patterns, indicating the absence of long-range ordering between Ni and Sn. To track feasible intra-inter layer cationic migration, HAADF-STEM images were collected (Figure 2c), but no Ni/ Sn were observed in

the sodium layer. STEM- EDX mapping (Figure 2d) on the crystallites shows that the Na, Sn, and Ni ions are homogeneously distributed in nano- and micrometer scale. The average composition over all measured crystallites is $Na_{1.09}Ni_{0.41}Sn_{0.51}O_2$ which is close to the $Na_{1.05}Ni_{0.45}Sn_{0.5}O_2$ stoichiometry expected from the synthesis batch.

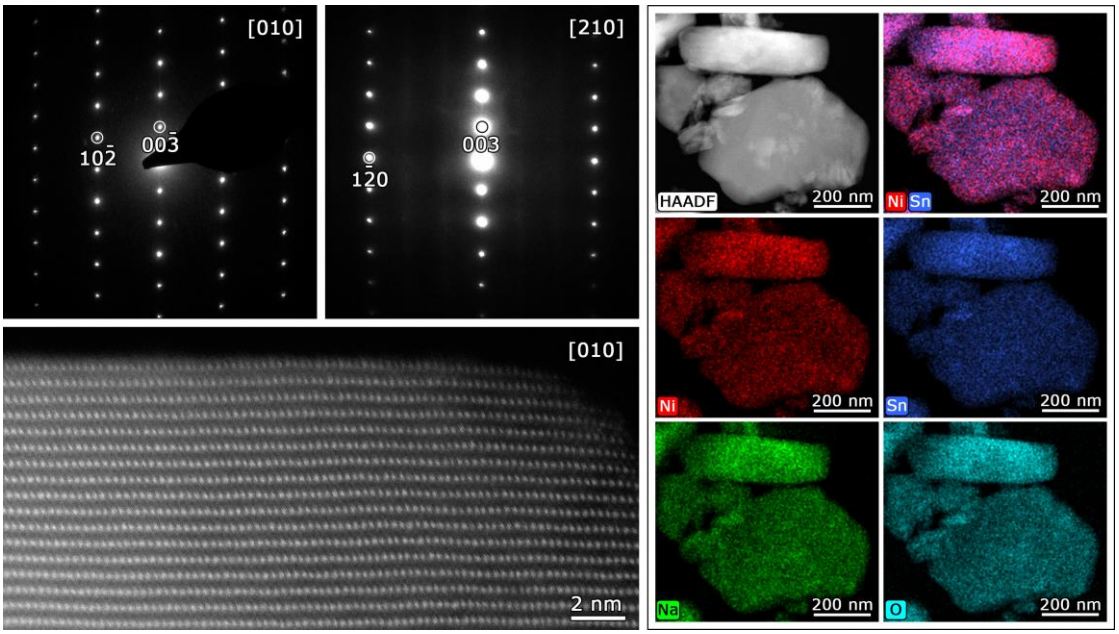

Figure 2: (a-d) Electron microscopy analysis details of $NaNi_{0.5}Sn_{0.5}O_2$; (a,b) electron diffraction pattern in [010] and [210] zones, (c) HAADF- STEM image to show the absence of cation intermixing between Na and MO_2 layers, (d) STEM- EDX images to show uniform distribution of Na, Ni, Sn and O.

Single-phase members of the $NaNi_{0.5}Mn_{0.5-y}Sn_yO_2$ series were first electrochemically tested in sodium half cells that were started in oxidation and cycled over the 4 to ~2.5 V potential window at a C/10 rate (**Figure 3a**). For the Sn-free $NaNi_{0.5}Mn_{0.5}O_2$ phase (y=0) the charge/discharge voltage profile shows a stair-case type variation associated to multiple phase transitions as previously reported.[10] Such accidental profile smoothens with increasing the Sn^{4+} substitution as shown on the derivative dQ/dV plots (Figure 3b). This is indicative of the progressive disappearance of the structural transitions with the tin end-member $NaNi_{0.5}Sn_{0.5}O_2$ showing a single sharp oxidation peak at ~3.2 V. Another striking feature of the Sn-based compounds (Figure 3b) is nested in their redox potential. It increases with

increasing the Sn^{4+} substitution, from 2.8 V for $NaNi_{0.5}Mn_{0.5}O_2$ to 3.2 V for the fully substituted $NaNi_{0.5}Sn_{0.5}O_2$. The equilibrium potential of $NaNi_{0.5}Sn_{0.5}O_2$ was also confirmed by Galvanostatic Intermittent Titration Technique (GITT) as shown in supporting information Figure S3.

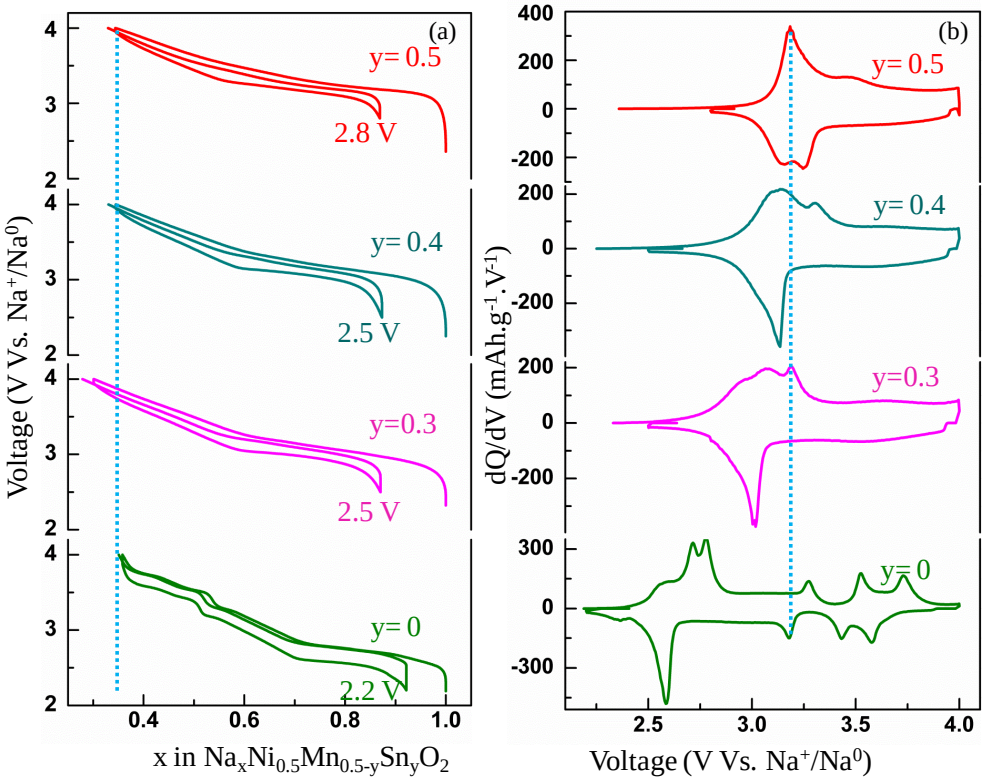

Figure 3: (a) Galvanostatic charge - discharge profile and the (b) corresponding derivative plots of the $NaNi_{0.5}Mn_{0.5-y}Sn_yO_2$ (y= 0, 0.3-0.5) in sodium half cells. The blue line in (a) and (b) are guide to eyes to show the amount of sodium de-inserted and the change in the redox potential respectively.

Altogether the Sn substitution in $NaNi_{0.5}Mn_{0.5}O_2$ increases the redox potential and minimizes phase transitions during cycling. Moreover, independently of the Mn/Sn ratio, all electrodes show a reversible uptake/release of nearly ~0.6 Na per unit formula within the error limit of the experimental data. It results that both Sn-free $NaNi_{0.5}Mn_{0.5}O_2$ and Mn-free $NaNi_{0.5}Sn_{0.5}O_2$ compounds show very similar energy densities (390 vs. 340 Wh/kg) since the voltage advantage provided by the Sn substitution (0.4 V) is negated by the capacity penalty

(100 vs. 120 mAh/g) due to the higher molecular weight of Sn compare to Mn (supporting information Figure S4).

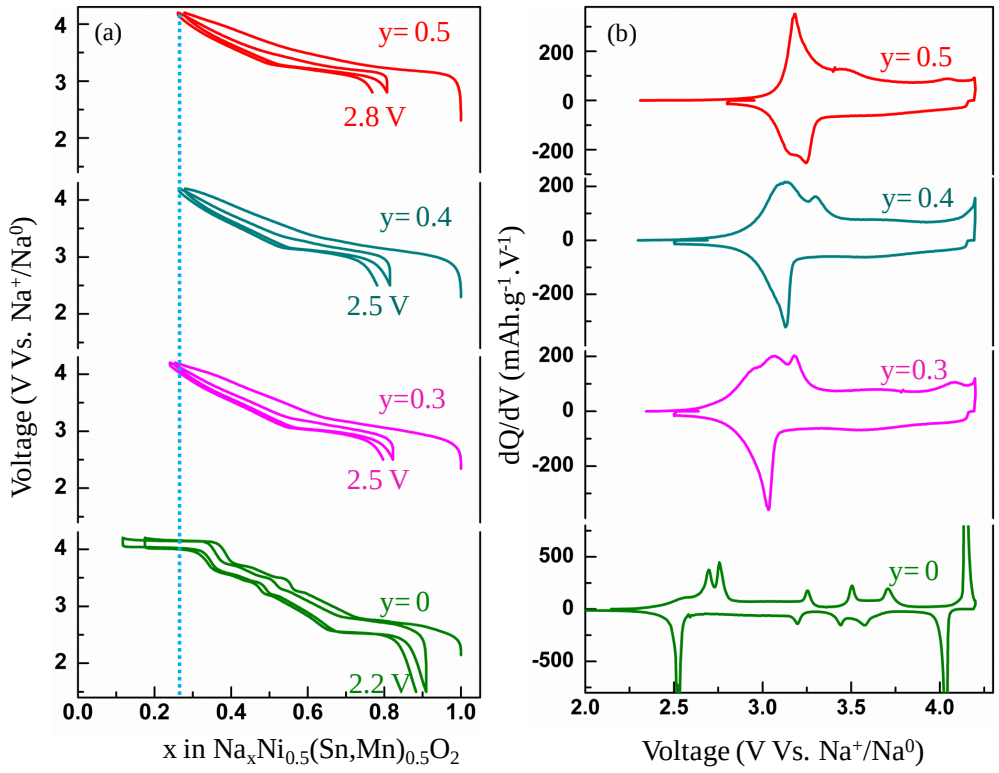

Figure 4: (a) Galvanostatic charge- discharge profile and the (b) corresponding derivative plots of the $NaNi_{0.5}Mn_{0.5-y}Sn_yO_2$ (y= 0, 0.3-0.5) half cells cycled between 4.2 V and the reduction voltage mentioned in the figure. The blue line in (a) is a guide to eyes to show the amount of sodium de-inserted.

We further show that by raising the charge cutoff voltage to 4.2 V, nearly ~0.9 sodium per unit formula can be removed from $NaNi_{0.5}Mn_{0.5}O_2$. The top part of the charging curve (**Figure 4a**) reveals the appearance of a new plateau at 4.2 V whose amplitude decreases with cycling, resulting in poor capacity retention (see supporting information Figure S5). Such a decay is minimized for the Sn-rich materials ($NaNi_{0.5}Mn_{0.5-y}Sn_yO_2$, y= 0.5, 0.4 and 0.3) which do not show the 4.2 V plateau.

To test the structural stability of the Sn-substituted phases against oxidation, we have carried out *in-situ* XRD analysis of the $NaNi_{0.5}Sn_{0.5}O_2$ by charging the material to 4 V during the first cycle and to 4.2 V on the following cycle. The collected XRD patterns reported in

Figure 5a indicate a thorough reversibility of the pristine structure irrespective of the voltage window used. Moreover, it is solely after the removal of ~0.5 sodium that the pristine O3 phase undergoes a phase transition from O3 to P3 phase via a biphasic process occurring over a narrow Na composition domain (<0.05). This is in total contrast with the poor structural stability of O3 $NaNi_{0.5}Mn_{0.5}O_2$ which fully transforms into the P3 phase after the removal of solely 0.2 sodium (Supporting information Figure S6).

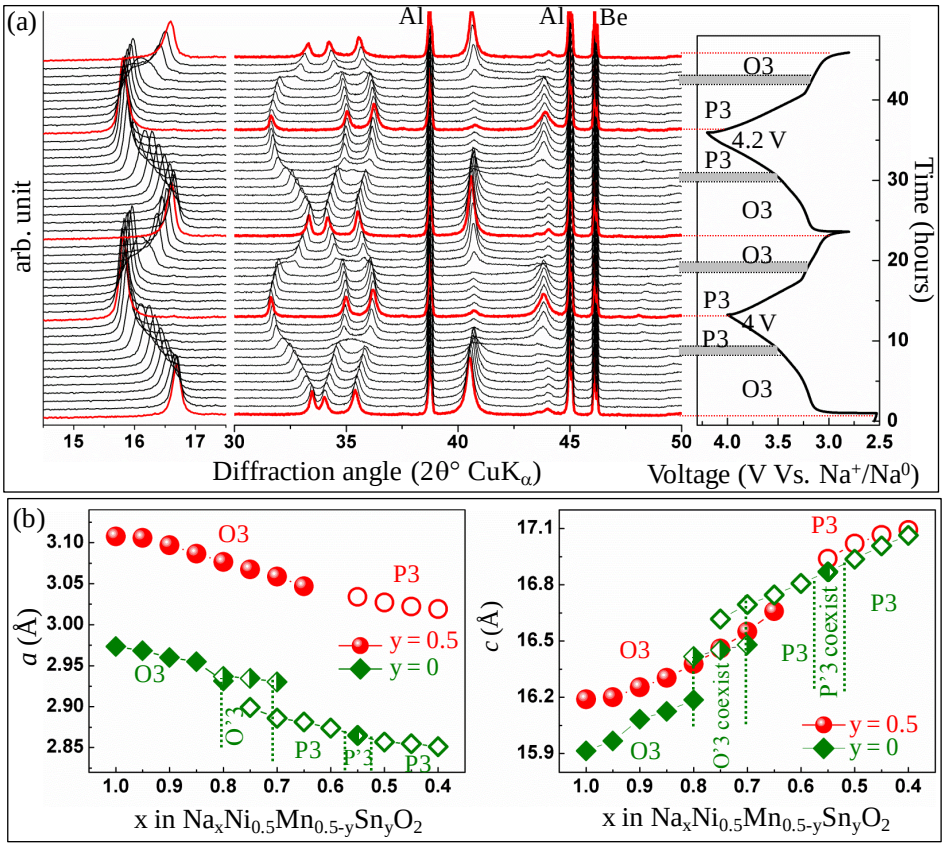

Figure 5: (a) *In-situ* XRD patterns of the $NaNi_{0.5}Sn_{0.5}O_2$ in sodium half cell when the cell is cycled between 4-2.8 V and 4.2-2.8 V in the first and second cycle, respectively. The evolution of O3 and P3 phases during charge-discharge processes are marked in the figure and the solid bar represents the small biphasic region (Δx = 0.05) in which O3 and P3 phases co-exist. (b) Lattice parameter evolution of $Na_xNi_{0.5}Sn_{0.5}O_2$ (red circles) and $Na_xNi_{0.5}Mn_{0.5}O_2$ (green diamonds) as a function of x. The lattice parameter of $Na_xNi_{0.5}Mn_{0.5}O_2$ is derived from the *in-situ* XRD pattern shown in supporting information Figure S6.

The evolution of the lattice parameters, during the first charge and discharge of an *in-situ* XRD Na/$Na_xNi_{0.5}Sn_{0.5}O_2$ cell is plotted in Figure 5b as a function of the Na content x together with those deduced from *in-situ* X-ray measurements of the Na/$Na_xNi_{0.5}Mn_{0.5}O_2$ half-cell cycled under the same conditions. Note that the *c* lattice expansion observed upon charging $Na_xNi_{0.5}Sn_{0.5}O_2$ and $Na_xNi_{0.5}Mn_{0.5}O_2$ is indicative of an increased O-O repulsion between the MO_2 layers during sodium removal.[9] Larger amounts of Na^+ are removed from $Na_xNi_{0.5}Sn_{0.5}O_2$ as compared to $Na_xNi_{0.5}Mn_{0.5}O_2$ (0.5 vs. 0.1 Na^+) before the gliding of the MO_2 layers is triggered. Lastly, both samples show a monotonous decrease of the *a* lattice, as expected from the metal ion oxidation and the resulting size contraction.

To evaluate the attractive performance of the $NaNi_{0.5}Mn_{0.5-y}Sn_yO_2$ samples associated with the improved structural stability provided by Sn^{4+} substitution, we have assembled sodium ion full cells using Hard carbon as negative electrode (**Figure 6**). All cells show nearly the same Na^+ uptake/release (~0.5 sodium per formula unit) with an average voltage that progressively increased from 2.8 V for pure manganese (y=0) to 3.01, 3.05 and 3.1 V for y= 0.3, 0.4 and 0.5 as deduced by dividing the total cell energy by specific capacity.

The energy density of the materials in Figure 6b shows a maximum of 335 $Wh.kg^{-1}$ for the lightest $NaNi_{0.5}Mn_{0.5}O_2$ electrode and relatively lesser 290, 280 and 270 $Wh.kg^{-1}$ for the heavier Sn-substituted electrodes. However, the capacity retention for the same cells in Figure 6c shows an excellent capacity retention exceeding 85% after 200 cycles for the Sn-rich phases $NaNi_{0.5}Mn_{0.5-y}Sn_yO_2$, y= 0.5-0.3 as compared to ~ 74% for the Sn-free $NaNi_{0.5}Mn_{0.5}O_2$ phase; all materials showed a coulombic efficiency of > 99.5% (Supplementary information Fig. S7). Such drop in cycle life for $NaNi_{0.5}Mn_{0.5}O_2$ is mainly associated with the partial irreversibility of the phase transition on continuous cycling, as explained in supporting information Figure S8. The $NaNi_{0.5}Mn_{0.5}O_2$ is additionally penalized application-wise by delivering 40% of its capacity at voltages lower than 2.5 V. At this stage, the best compromise in terms of electrode composition is $NaNi_{0.5}Mn_{0.1}Sn_{0.4}O_2$ that shows a reversible capacity of

91 mAh.g^{-1} (2 to 3.8 V vs. Hard carbon) and an energy density of 280 Wh.kg^{-1} (cell voltage= 3.05 V) with a capacity retention of 85 % after 200 cycles.

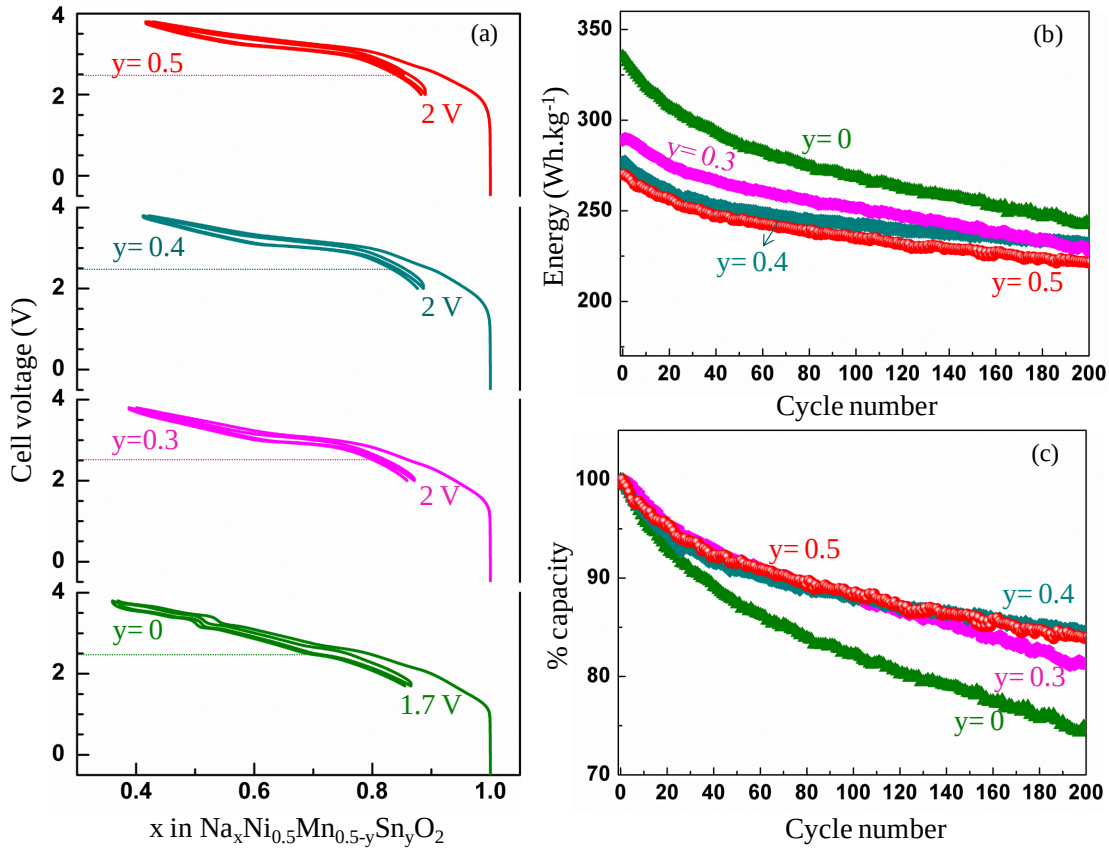

Figure 6: (a) Galvanostatic charge- discharge profile of NaNi$_{0.5}$Mn$_{0.5-y}$Sn$_y$O$_2$ (y= 0, 0.3-0.5) in sodium ion full cells using hard carbon negative electrode. The cells were cycled in the voltage window of 3.8- 2 V; discharge potential of 1.7 V is used only for NaNi$_{0.5}$Mn$_{0.5}$O$_2$ owing to its redox process at low voltage (~2.5 V vs. Na$^+$/Na^0) (b) Energy density and (c) capacity retention of NaNi$_{0.5}$Mn$_{0.5-y}$Sn$_y$O$_2$ (y= 0, 0.3-0.5) as a function of cycle number; the first discharge capacities of 118, 96, 91 and 88 mAh.g^{-1} are taken as 100% capacity for the materials with y= 0, 0.3, 0.4 and 0.5 respectively.

These results show that the substitution of Mn^{4+} by Sn^{4+} in NaNi$_{0.5}$Mn$_{0.5}$O$_2$ increases the redox potential and suppresses some phase transitions, with this release in structural strain being beneficial to the material lifecycle. In order to rationalize the impact of Sn substitution on the structural and electronic structures of NaNi$_{0.5}$Sn$_{0.5}$O$_2$ and NaNi$_{0.5}$Mn$_{0.5}$O$_2$, DFT

calculations were performed by first exploring changes in the Ni-O bond ionicity due to the ancillary metal ion (Sn^{4+} vs. Mn^{4+}).

Firstly, the Bader charges on Ni and O for both $NaNi_{0.5}Sn_{0.5}O_2$ and $NaNi_{0.5}Mn_{0.5}O_2$ phases were calculated by DFT as a function of the Ni-O distance using three structural models with different cations ordering (supporting information S9(a)). By plotting their difference, which is an indicator of the bond ionicity (**Figure 7a**), we observe a large increase in Ni-O bond ionicity on moving from Mn^{4+} ($NaNi_{0.5}Mn_{0.5}O_2$) to Sn^{4+} ($NaNi_{0.5}Sn_{0.5}O_2$) irrespective of Ni/Mn and Ni/Sn cationic ordering and bond distance used for the calculation. Since Ni Bader charge stays constant, this indicates a higher electronic density on oxygen in $NaNi_{0.5}Sn_{0.5}O_2$ compared to $NaNi_{0.5}Mn_{0.5}O_2$. Such an increase in the electronic density on oxygen stabilizes the O 2*p* orbital which implies an increase in the energy difference between Ni 3*d* and O 2*p* orbitals (Figure 7b) and by the same token an increase of the Ni-O bond ionicity and redox potential.[15] To better understand such increased charge density on oxygen with Sn^{4+} substitution, the projected Density of States (pDOS) is drawn for $NaNi_{0.5}Sn_{0.5}O_2$ and $NaNi_{0.5}Mn_{0.5}O_2$ (Figure 7c). In the case of the $NaNi_{0.5}Mn_{0.5}O_2$, we observe an overlap between Ni, Mn and O states near the Fermi level, signature of a covalent system with delocalized electrons. On the contrary, in $NaNi_{0.5}Sn_{0.5}O_2$, electron delocalization in the metallic layers is partially lost due to the absence of interacting *d* orbitals. This indicates Sn – O forms an ionic bond leading to a higher charge on the oxygen, as computed for the Sn substituted compounds. The average voltages computed for $NaNi_{0.5}Sn_{0.5}O_2$ and $NaNi_{0.5}Mn_{0.5}O_2$ are systematically higher for the Sn-substituted material, whatever is the cationic order considered in the structure and is in good agreement with our experimental results (see supporting information S9(a)). One should notice that these findings correlate well with the well-known inductive effect[17] since the charge (δ-) on oxygen is increased by Sn substitution, hence leading to a higher redox potential. Nevertheless, in the present case, the increase in "oxygen electronegativity" is not due to the formation of X-O covalent bonds, as

in polyanionic systems[17] but arises from the narrowing of the metallic bands due to less efficient *d-d* overlap in the metallic layer.

DFT calculations were also used to get some insights into the origin of the delayed O3 – P3 transition and the suppression of the O'3 and P'3 phases during Na removal in $NaNi_{0.5}Sn_{0.5}O_2$ as compared to $NaNi_{0.5}Mn_{0.5}O_2$. From previous literature, it is well established that O3 phase having reduced O-O interactions is the most stable among the O3 and P3 phases with therefore the feasibility to stabilize the P3 phase by favoring Na-Na ordering and hence minimizing the Na-Na repulsion.[11] Thus, the relative energies of P3-$Na_xNi_{0.5}Mn_{0.5}O_2$ and P3-$Na_xNi_{0.5}Sn_{0.5}O_2$ phases were computed for different Na-ordering leading to different Na-Na distances and different Na-M environments (see supporting Information S9(b) for calculation details). First we considered (i) Na in the triangular lattice which is quite similar to the Na arrangement in O3 phase (Na-Na distance= a= 3 Å) and (ii) Na in the hexagonal lattice that is specific to the P3 phase (Na-Na distance= $a^*(2/\sqrt{3})$= 3.5 Å).[13] The results show (Figure 7d) that the Na ordering with higher Na – Na distance (≈ 3.5 Å) is slightly preferred (small energy gains ~ 15 meV/F.U) to the one with smaller Na – Na distance (3 Å), for both Sn- and Mn-substituted materials. Such a stabilization of the P3 structure with Na ordering contrasts with the results obtained for different Na-environments namely (i) Na in Ni-rich environment (Na shares one face and two edges with Ni and one edge with Mn/Sn) and (ii) Na in Mn/Sn-rich environment (Na shares one face and two edges with Mn/Sn and one edge with Ni). The P3 $Na_{0.5}Ni_{0.5}Sn_{0.5}O_2$ structure having Na in Sn-rich environment (Figure 7e) is now highly destabilized compared to Ni-rich environment ($|\Delta E|$ ~ 45 meV/F.U.) showing that Na prefers sites with Ni-rich environment in presence of Sn. This site discrimination is not observed in $Na_{0.5}Ni_{0.5}Mn_{0.5}O_2$ phases, where both Ni-rich and Mn-rich environments leads to equivalent energies within 5 meV/F.U difference. Having shown experimentally that Sn is disordered in the structure by STEM (fig. 2), such Sn driven occupation of Na in $Na_{0.5}Ni_{0.5}Sn_{0.5}O_2$ reduces the P3 phase stability which was shown to stabilize by Na-Vacancy

ordering as reported previously. It delays the O3⇔P3 phase transition till the removal of ~0.5 Na for $NaNi_{0.5}Sn_{0.5}O_2$ in comparison to 0.2 Na for $NaNi_{0.5}Mn_{0.5}O_2$. The phase transitions to P'3 and O'3 have been reported to be triggered by concomitant Jahn-Teller distortions and Na ordering.[18] Since Ni^{3+} Jahn Teller distortion is feasible in both Mn^{4+} and Sn^{4+} substituted compounds, the suppression of these phase transitions in the Sn compound ($NaNi_{0.5}Sn_{0.5}O_2$) is mainly related to the absence of cooperative Na ordering for reasons mentioned above.

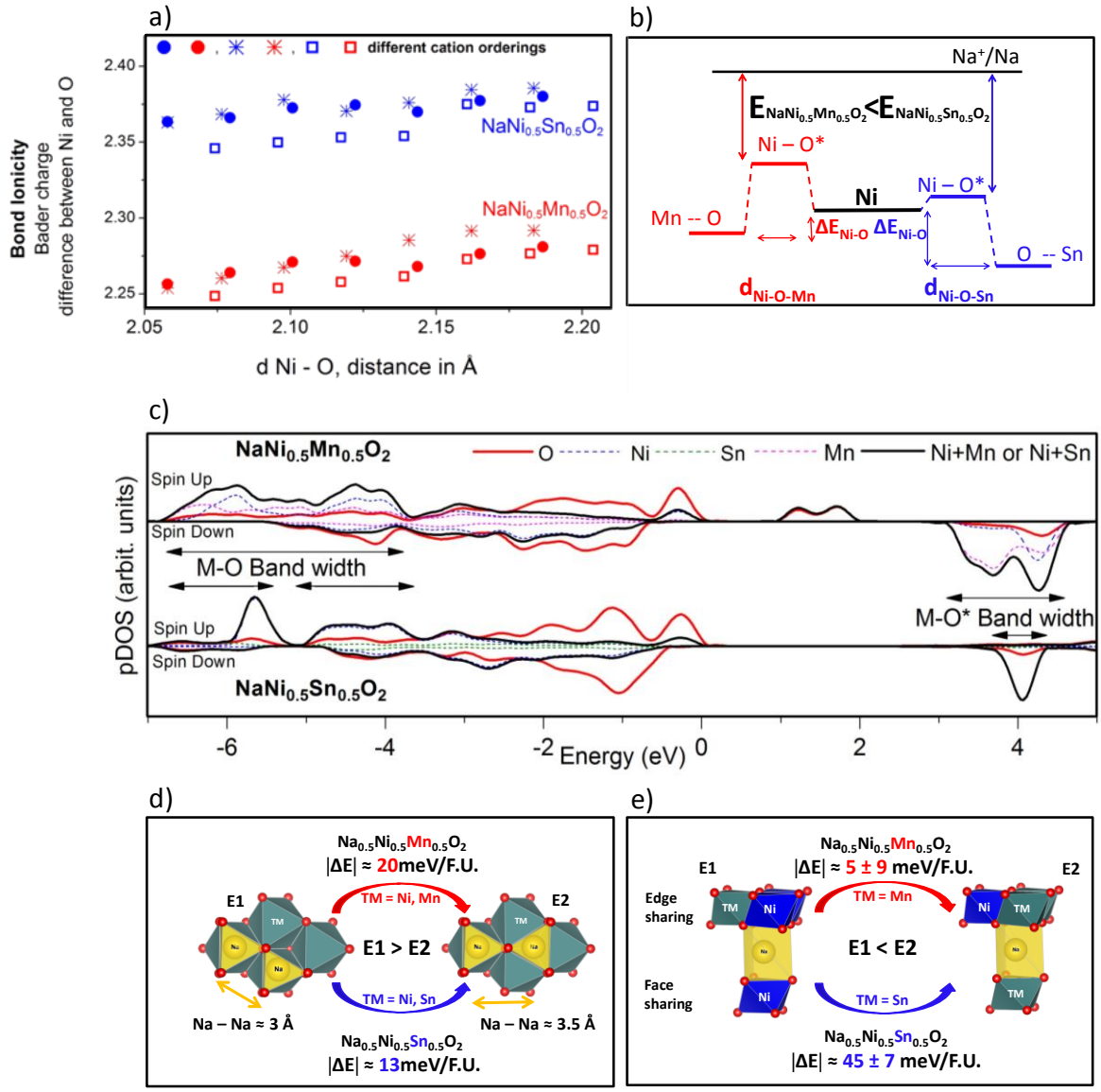

Figure 7: (a) Difference between Bader charge, obtained by DFT calculation, of Ni and O depending on the Ni – O distance in Å, tuned with the cell volume, for $NaNi_{0.5}Sn_{0.5}O_2$ in blue and $NaNi_{0.5}Mn_{0.5}O_2$ in red. Square, stars and dots stand for different Ni/Sn and

Ni/Mn cation orderings. b) Molecular orbital diagram for Ni – O in the case of $NaNi_{0.5}Sn_{0.5}O_2$ on the right, in blue, and $NaNi_{0.5}Mn_{0.5}O_2$, on the left part in red, showing why potential is increase when ΔE_{Ni-O} or d_{Ni-O} are increased. c) The projected density of state computed with PBE+U (U_{Ni} = 6eV and U_{Mn}=5eV) of $NaNi_{0.5}Mn_{0.5}O_2$ and $NaNi_{0.5}Sn_{0.5}O_2$ at the top and bottom respectively. It emphasizes the respective band width of M – O states in both compounds. d) and e) are schematics showing the energy gain/loss depending on the Na position. In d), 20meV for $Na_{0.5}Ni_{0.5}Mn_{0.5}O_2$ and 13 meV for $NaNi_{0.5}Sn_{0.5}O_2$ are gained moving from a Na position in which Na – Na distance is around 3Å to a Na position in which Na – Na is around 3.5Å. In e), 5meV for $Na_{0.5}Ni_{0.5}Mn_{0.5}O_2$ and 45 meV for $NaNi_{0.5}Sn_{0.5}O_2$ are lost going from a Na site which shares a face and two edges with Ni and one edge with Sn/Mn to a site in which Na shares a face and two edges with Sn/Mn and one edge with Ni.

Taken together these results indicate that Sn^{4+}, owing to its large size and its tendency to favor electron localization in the metallic layer, increases the redox potential and delays the Na-driven phase transitions in Na-based layered oxides having the O3 structure. It is now of interest to check whether this strategy based on the use of chemical substituents with a filled *d* ($4d^{10}$) band can be generalized to other metals having no available *d* orbitals for M-O bonding such as Ge^{4+} ($3d^{10}$), Ti^{4+} ($3d^0$), Zr^{4+} ($4d^0$). The Bader charge calculation on $NaNi_{0.5}M'_{0.5}O_2$ with M' being Ge^{4+} ($3d^{10}$), Ti^{4+} ($3d^0$), Zr^{4+} ($4d^0$) shows charge localization and increased charge density on oxygen in comparison to the Mn substituent (Supporting Information Figure S10). From Bader charge analysis, the compounds can be ranked as follows, $NaNi_{0.5}Zr_{0.5}O_2$ > $NaNi_{0.5}Ge_{0.5}O_2$ ≈ $NaNi_{0.5}Sn_{0.5}O_2$ > $NaNi_{0.5}Ti_{0.5}O_2$ > $NaNi_{0.5}Mn_{0.5}O_2$ with $NaNi_{0.5}Ti_{0.5}O_2$ having the lowest Ni-O bond ionicity among the studied d^0 and d^{10} materials due to partial delocalization of Ti *d* orbitals as shown in Figure S9(b). Interestingly, and in agreement with this prediction, the substitution of Mn^{4+} by Ti^{4+} (r_{Ti}^{4+} (0.6 Å)) which is smaller than Sn^{4+}, therefore to provide better capacity, was shown to lead to a slight increase of

potential.[19, 20] However, the reported O3 $NaNi_{0.5}Ti_{0.5}O_2$ phase is quite less stable and the removal of solely 0.2 Na is sufficient to trigger the O3-P3 phase transformation as compared to 0.5 for the Sn series.[19] This emphasizes the complexity in finding the perfect trade-off between redox potential and phase stability to tune the O3-$Na(NiM)O_2$ phases and the success associated with the Sn^{4+} substitution in solving both the issues.

Going further, we tried to address the two other recurrent problems of the layered O3 $NaMO_2$ phases, namely (i) poor rate capability and (ii) moisture sensitivity. Usually, the O3 $NaMO_2$ phases show limited rate capability and this is explained by considering the sodium ion diffusion path between two octahedral sites which needs to go through an intermediate tetrahedral site viewed as a bottleneck.[21] Additionally, the various phase transitions triggered by the removal of Na-ions from the O3 structures create different phase boundaries that could further penalize the electrode impedance. However, we hypothesize this effect to be minimum with the $NaNi_{0.5}Sn_{0.5}O_2$ system since it undergoes a single O3 ⇔ P3 phase transition through Na removal. However, considering the complexity in calculating the ionic and electronic conductivities as a function of x in $Na_xNi_{0.5}Sn_{0.5}O_2$, we relied on rate capability measurements to indirectly provide some insights into this issue. These measurements performed on two Na half cells containing either $NaNi_{0.5}Sn_{0.5}O_2$ or $NaNi_{0.5}Mn_{0.5}O_2$ as positive electrodes show nearly the similar rate capability that is the maintenance of ~80 % of the capacity even at 1C rate (**Figure 8a**). This suggests that the Sn-driven charge localization in $Na_xNi_{0.5}Sn_{0.5}O_2$ reduces the electronic conduction of the material (supplementary information Fig. S11) and hence significantly affect the power rate capability.

Lastly, to analyze the moisture sensitivity of $NaNi_{0.5}Sn_{0.5}O_2$, we have exposed the material to moist air with a relative humidity (RH) of 60 % and recorded the evolution of its XRD pattern as a function of time. No observable change in XRD pattern was obtained till one hour of exposure, however a new phase whose structure is quite similar to that of

birnessite, having water molecule in between the layers, starts to appear on prolonged exposure (>3 hours) (Figure 8b).[22]

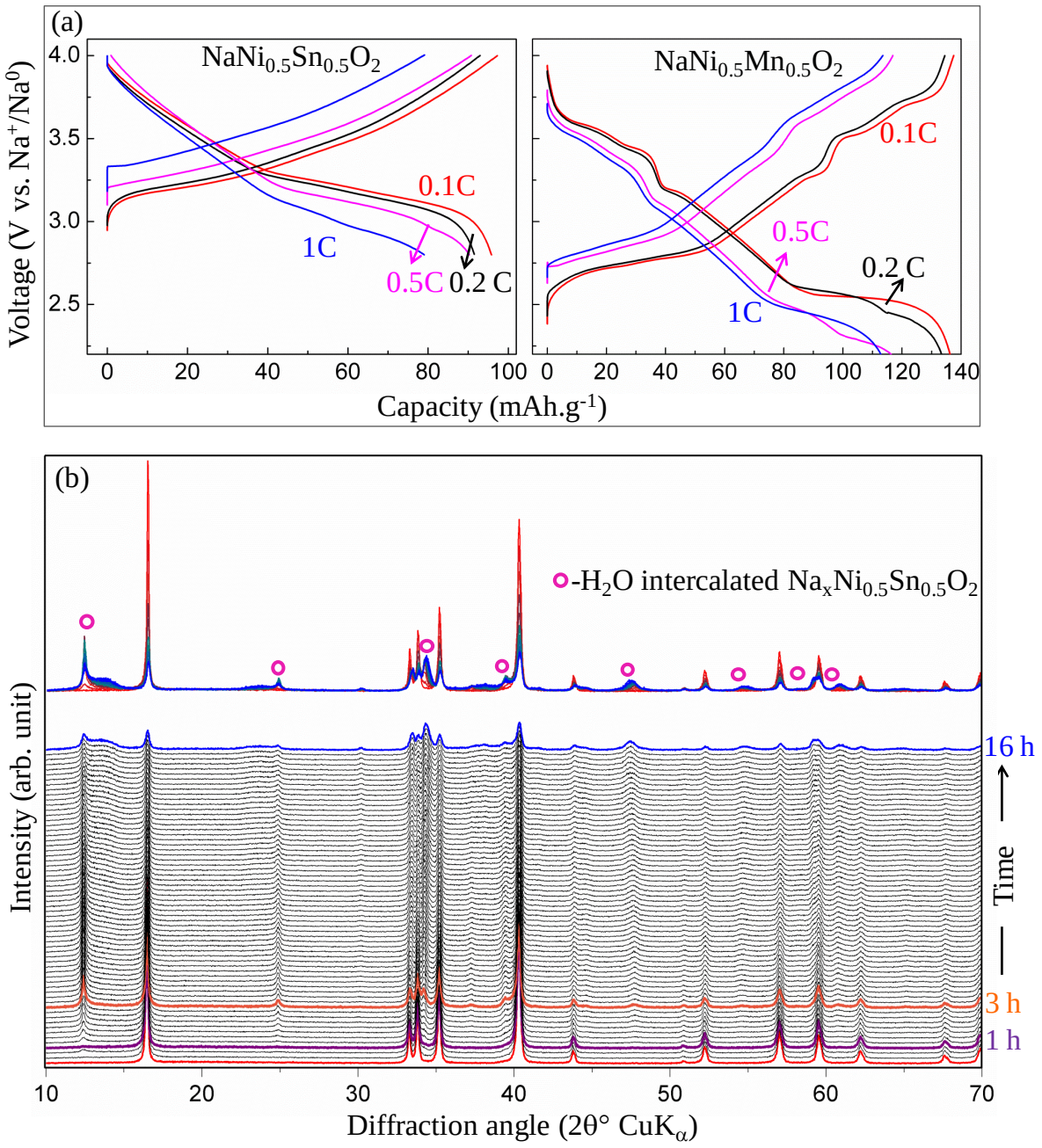

Figure 8: (a) Second cycle galvanostatic charge- discharge profiles of (left) $NaNi_{0.5}Sn_{0.5}O_2$ vs. Na and (right) $NaNi_{0.5}Mn_{0.5}O_2$ vs. Na half cells cycled at different rates. (b) Evolution of $NaNi_{0.5}Sn_{0.5}O_2$ on exposure to moist air (RH≈ 60%). Each XRD pattern corresponds to the air exposure of 15 min; top part is the combined image of the bottom panel to show the initial and final phase with the intermediates.

Such Na^+/H_3O^+ exchange or H_2O insertion could be facilitated due to the increased interlayer distance of Sn-substituted materials. The water uptake for the 3 hours exposed sample was confirmed by thermo gravimetric analysis (TGA) coupled with Mass spectrometry which show two weight losses at 150 °C and > 300 °C associated with the departure of H_2O (M/z = 18) and CO_2 (m/z = 44), respectively (supporting information Figure S12). Thus, powders of electrodes made out of the $NaNi_{0.5}Sn_{0.5}O_2$ phases, in spite of their elevated (3.2 V) redox potential, will have to be handled in dry conditions.

This result is somewhat intriguing in light of recent literature results claiming that copper substitution increases the redox potential of layered Na-based materials to 3.2 V while enhancing their moisture stability.[23] Interesting questions remain to be answered in this context: What is the specific role of Cu and how can it affects the acid-basicity of the materials surface and why is Sn more prone to hydration? Answering these questions call for setting a reliable experimental protocol to benchmark various Na-based layered phases against reactivity towards moisture so as to define trends. This is critical for the predictive design of novel water stable Na-based layered oxide electrodes.

3. Conclusion

We have reported the chemical substitution of Mn^{4+} by larger and (d^{10}) non transition metal ion such as Sn^{4+} in O3-$NaNi_{0.5-y}Mn_yO_2$ as an attractive strategy to simultaneously increase the redox voltage and delay the O3 ⇔ P3 phase transition during cycling. The fully substituted $NaNi_{0.5}Sn_{0.5}O_2$ phase shows a redox potential of ~3.2 V vs. Na^+/Na^0 as compared to solely 2.8 V for $NaNi_{0.5}Mn_{0.5}O_2$. Moreover, the Sn-based phase was found to show enhanced stability against the O3 ⇔ P3 transformation which did not occur till the removal of 0.5 sodium from the structure as compared to 0.2 for the Mn-based phase. Among the series $NaNi_{0.5}Mn_{0.5-y}Sn_yO_2$ (y= 0- 0.5), the composition $NaNi_{0.5}Mn_{0.1}Sn_{0.4}O_2$ was practically-wise identified as the most interesting owing to its capacity (91 $mAh.g^{-1}$), energy density (280 $Wh.g^{-1}$) and capacity

retention (85% after 200 cycles). Nevertheless, a remaining hurdle pertaining to this Sn-based phase is still its moisture sensitivity. Understanding and solving this water reactivity is quite complex, but worth it to spend some time owing to the practical interest that such phases could offer. Looking forward, it will also be of great interest to systematically investigate the effects of chemical substitutions having (d^0) and (d^{10}) configuration shells.

4. Experimental

4.1. Synthesis: All compounds were prepared by solid state synthesis. The metal oxides manganese (IV) oxide (MnO_2, Aldrich), nickel (II) oxide (NiO, Aldrich), tin (IV) oxide (SnO_2, Aldrich) and sodium carbonate (Na_2CO_3, Aldrich) were mixed in their respective stoichiometric ratio and homogenized by hand grinding for 20 min. The homogenized powders were ball-milled for 1 hour in spex mixer mill with the material to balls ratio of 1: 20 by weight. The ball-milled precursor mixture is heated in air at 850 °C for 12 hours followed by regrinding and calcinations in argon at 900 °C for 12 h. The heating and cooling rates were maintained at 5 and 1°C/ min respectively. The second calcination step is carried out in argon in order to avoid the materials exposure to air during cooling.

4.2. Structural characterizations: The recovered materials were analyzed by powder X-ray diffraction analysis (XRD) in Bruker D8 advanced diffractometer using Cu K_α radiation source. The powder XRD patterns were refined using Fullprof program.[24] High resolution TEM analysis was performed in a FEI Titan^3 cubed microscope operated at 200-300 kV. EDX-STEM analysis was done using a super-X detector on the FEI Titan^3, as well as on a FEI Osiris TEM. The specimen for TEM was prepared by grinding it using an agate mortar and pestle in an argon filled glove box and putting it on a copper grid covered with holey carbon. It was subsequently transferred to the TEM chamber using a Gatan vacuum transfer holder, preventing contact with air.

4.3. Electrochemical characterizations: Electrochemical tests were carried out in Swagelok type sodium half cells and CR2032 coin cells for full cell studies. Powder $NaNi_{0.5}Mn_{0.5-y}Sn_yO_2$ ball milled with 15% carbon is used as positive electrode without any binder additive. Sodium metal, pressed into a stainless-steel current collector disc is used as negative electrode for half cells. Hard carbon electrode of mass ~5.5 mg/ cm^2 coated on aluminum foil is used as negative electrode for full cell studies. In both cases we used an electrolyte made by dissolving 1M $NaPF_6$ (sodium hexa fluoro phosphate) in PC (propylene carbonate), with in the case of half cells the addition of 3% FEC (fluoro ethylene carbonate) by weight. The cycling rates were calculated using the theoretical capacity of the material for removing 1 sodium as 1 C.

4.4. DFT+ U calculations: Spin-polarized density functional theory (DFT) calculations were performed using the plane-wave density functional theory VASP (Vienna ab initio simulation package) code[25] within the generalized gradient approximation of Perdew−Burke−Ernzerhof (PBE) to describe electron exchange and correlation[26]. The rotationally invariant Dudarev method (DFT + U)[27] was used to correct the self-interaction error of conventional DFT for correlated *d*-electrons. All calculations were performed on a structural model constructed with one layer of 8 Na and one layer of 8 TM (TM = Ni, Sn or Mn). Three different cation orderings were considered among the Ni/Sn and Ni/Mn distributions. For structural relaxation, the conjugate gradient method was used until the energy varies by less than 0.1 meV and the atomic forces by less than 0.02 eV/$Å^3$. Plane-wave cut-off of 600 eV was used and a 3x6x6 Monkhorst pack sampling for Brillouin zone integration.

Supporting Information

Supporting Information 12 figures showing the structure, capacity retention, etc., and crystallographic information table are available from the Wiley Online Library or from the author.

Acknowledgements

[†]M. S and Q. J contributed equally to this work.

The authors thank Dr. Daniel Alves Dalla corte and Sujoy Saha for electronic conductivity measurements and Prof. Dominique Larcher for fruitful discussions. Q.J. thanks the ANR "Deli-Redox" for Ph.D. funding. J.-M.T. acknowledges funding from the European Research Council (ERC) (FP/2014)/ERC Grant-Project 670116-ARPEMA. TGA analysis by Matthieu Courty, LRCS, Amiens is greatly acknowledged.

Received: ((will be filled in by the editorial staff))
Revised: ((will be filled in by the editorial staff))
Published online: ((will be filled in by the editorial staff))

References

[1] P. Rozier, J. M. Tarascon, *J. Electrochem. Soc.* **2015**, *162*, A2490; W. Li, B. Song, A. Manthiram, *Chem. Soc. Rev.* **2017**, *46*, 3006.

[2] D. Larcher, J. M. Tarascon, *Nat Chem* **2015**, *7*, 19.

[3] J.-Y. Hwang, S.-T. Myung, Y.-K. Sun, *Chem. Soc. Rev.* **2017**, *46*, 3529; H. Kim, H. Kim, Z. Ding, M. H. Lee, K. Lim, G. Yoon, K. Kang, *Adv. Energy Mater.* **2016**, *6*, 1600943.

[4] Y. Liu, X. Liu, T. Wang, L.-Z. Fan, L. Jiao, *Sustainable Energy & Fuels* **2017**, *1*, 986.

[5] J. Cabana, L. Monconduit, D. Larcher, M. R. Palacín, *Adv. Mater.* **2010**, *22*, E170; Y. Lei, X. Li, L. Liu, G. Ceder, *Chem. Mater.* **2014**, *26*, 5288; Y. Tang, Y. Zhang, W. Li, B. Ma, X. Chen, *Chem. Soc. Rev.* **2015**, *44*, 5926.

[6] C. Delmas, J.-J. Braconnier, C. Fouassier, P. Hagenmuller, *Solid State Ion* **1981**, *3*, 165; M. H. Han, E. Gonzalo, G. Singh, T. Rojo, *Energy Environ. Sci.* **2015**, *8*, 81.

[7] X. Li, D. Wu, Y.-N. Zhou, L. Liu, X.-Q. Yang, G. Ceder, *Electrochem. Commun.* **2014**, *49*, 51; J.-Y. Hwang, C. S. Yoon, I. Belharouak, Y.-K. Sun, *J. Mater. Chem. A.* **2016**, *4*, 17952.

[8] I. Saadoune, A. Maazaz, M. Ménétrier, C. Delmas, *J. Solid State Chem.* **1996**, *122*, 111.

[9] M. Sathiya, K. Hemalatha, K. Ramesha, J. M. Tarascon, A. S. Prakash, *Chem. Mater.* **2012**, *24*, 1846.

[10] S. Komaba, N. Yabuuchi, T. Nakayama, A. Ogata, T. Ishikawa, I. Nakai, *Inorg. Chem.* **2012**, *51*, 6211.

[11] C. Delmas, C. Fouassier, P. Hagenmuller, *Physica B+C* **1980**, *99*, 81.

[12] J. Vinckevičiūtė, M. D. Radin, A. Van der Ven, *Chem. Mater.* **2016**, *28*, 8640.

[13] M. D. Radin, A. Van der Ven, *Chem. Mater.* **2016**, *28*, 7898.

[14] X. Xia, J. R. Dahn, *J. Electrochem. Soc.* **2012**, *159*, A1048; P.-F. Wang, Y. You, Y.-X. Yin, Y.-G. Guo, *J. Mater. Chem. A* **2016**, *4*, 17660; S. Komaba, A. Ogata, T. Shimizu, C. Takei, T. Nakayama, *Meeting Abstracts* **2008**, MA2008-02, 630.

[15] J. B. Goodenough, Molecular Crystals and Liquid Crystals Science and Technology. Section A. *Molecular Crystals and Liquid Crystals* **1998**, *311*, 1.

[16] L. Pauling, *J. Am. Chem. Soc.* **1929**, *51*, 1010.

[17] B. C. Melot, D. O. Scanlon, M. Reynaud, G. Rousse, J.-N. Chotard, M. Henry, J.-M. Tarascon, *ACS Applied Materials & Interfaces* **2014**, *6*, 10832.

[18] M. E. Arroyo y de Dompablo, G. Ceder, *J. Power Sources* **2003**, *119*, 654; X. Li, X. Ma, D. Su, L. Liu, R. Chisnell, S. P. Ong, H. Chen, A. Toumar, J.-C. Idrobo, Y. Lei, J. Bai, F. Wang, J. W. Lynn, Y. S. Lee, G. Ceder, *Nat Mater* **2014**, *13*, 586; P. Vassilaras, D.-H. Kwon, S. T. Dacek, T. Shi, D.-H. Seo, G. Ceder, J. C. Kim, *J. Mater. Chem. A* **2017**, *5*, 4596.

[19] X. Qi, Y. Wang, L. Jiang, L. Mu, C. Zhao, L. Liu, Y.-S. Hu, L. Chen, X. Huang, *Part Part Sys. Charact.* **2016**, *33*, 538.

[20] P.-F. Wang, H.-R. Yao, X.-Y. Liu, J.-N. Zhang, L. Gu, X.-Q. Yu, Y.-X. Yin, Y.-G. Guo, *Adv. Mater.* **2017**, *29*, 1700210.

[21] N. Yabuuchi, K. Kubota, M. Dahbi, S. Komaba, *Chem. Rev.* **2014**, *114*, 11636.

[22] Y. Li, X. Feng, S. Cui, Q. Shi, L. Mi, W. Chen, *CrystEngComm* **2016**, *18*, 3136; K. W. Nam, S. Kim, E. Yang, Y. Jung, E. Levi, D. Aurbach, J. W. Choi, *Chem. Mater.* **2015**, *27*, 3721.

[23] H.-R. Yao, P.-F. Wang, Y. Gong, J. Zhang, X. Yu, L. Gu, C. OuYang, Y.-X. Yin, E. Hu, X.-Q. Yang, E. Stavitski, Y.-G. Guo, L.-J. Wan, *J. Am. Chem. Soc.* **2017**, *139*, 8440; L. Mu, S. Xu, Y. Li, Y.-S. Hu, H. Li, L. Chen, X. Huang, *Adv. Mater.* **2015**, *27*, 6928; L. Zheng, J. Li, M. N. Obrovac, *Chem. Mater.* **2017**, *29*, 1623.

[24] J. Rodriguez-Carvajal, "FULLPROF: a program for Rietveld refinement and pattern matching analysis", presented at *satellite meeting on powder diffraction of the XV congress of the IUCr*, 1990; J. Rodriguez-Carvajal, Physica B: *Condensed Matter* **1993**, *192*, Pages 55.

[25] G. Kresse, J. Hafner, Physical Review B 1993, 47, 558; G. Kresse, J. Furthmüller, *Comput. Mater. Sci.* **1996**, *6*, 15.

[26] J. P. Perdew, K. Burke, M. Ernzerhof, *Phys. Rev. Lett.* **1996**, *77*, 3865.

[27] S. L. Dudarev, G. A. Botton, S. Y. Savrasov, C. J. Humphreys, A. P. Sutton, *Phys. Rev. B* **1998**, *57*, 1505.

The table of contents entry:

A cobalt free sodium layered oxide electrode material O3 $NaNi_{0.5}Sn_{0.5}O_2$ that shows long term cycling performance due to suppressed phase transitions, and high voltage (3.2 V) owing to the increase ionicity of the Mn-O bond via Sn substitution is identified.

Keyword: Sodium ion battery, O3-type layered oxide, phase transition, charge localization, redox potential

Authors:

*Mariyappan Sathiya,† Quentin Jacquet,† Marie-Liesse Doublet, Olesia M. Karakulina, Joke Hadermann and Jean-Marie Tarascon.**

A CHEMICAL APPROACH TO RAISE CELL VOLTAGE AND SUPPRESS PHASE TRANSITION IN O3 SODIUM LAYERED OXIDE ELECTRODES.

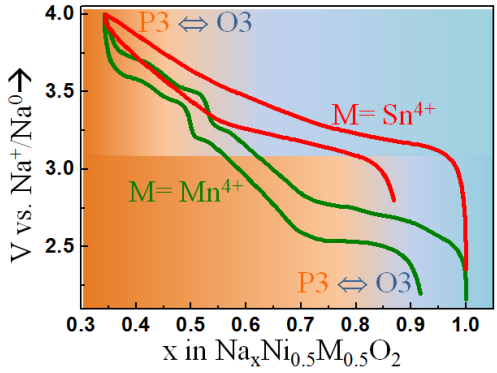

Supporting Information

A CHEMICAL APPROACH TO RAISE CELL VOLTAGE AND SUPPRESS PHASE TRANSITION IN O3 SODIUM LAYERED OXIDE ELECTRODES.

*Mariyappan Sathiya,[†] Quentin Jacquet,[†] Marie-Liesse Doublet, Olesia M. Karakulina, Joke Hadermann and Jean-Marie Tarascon.**

1. Supporting Information S-1

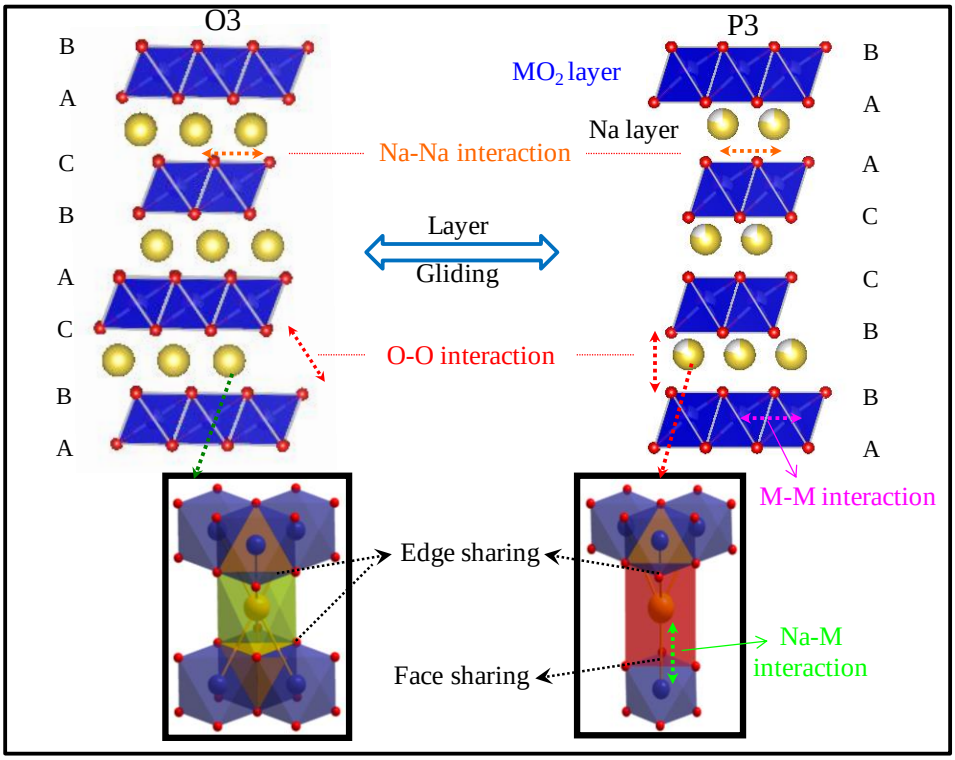

Figure. S1: Structure of O3 and P3 Na_xMO_2 ($0 < x < 1$), zoomed parts in the bottom showing the sodium occupation in octahedral and prismatic position of O3 and P3 phases respectively. Stability of the particular composition of Na_xMO_2 depends on the energies of the possible O-O, Na-Na, Na-M interactions mentioned in the figure.

2. Supporting Information S-2

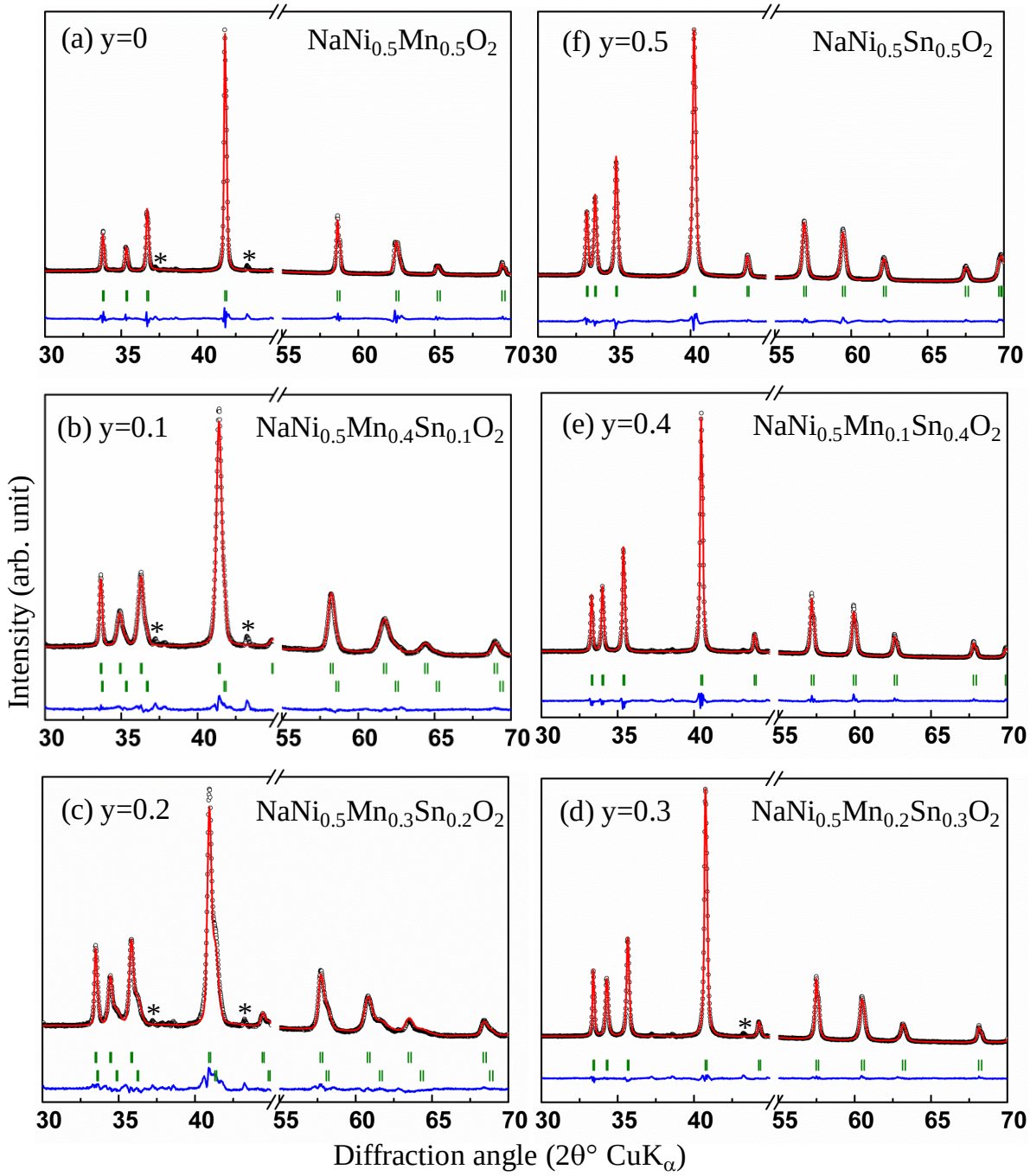

Figure. S2: Rietveld refined powder XRD pattern of the (a) $NaNi_{0.5}Mn_{0.5}O_2$ (b) $NaNi_{0.5}Mn_{0.4}Sn_{0.1}O_2$ (c) $NaNi_{0.5}Mn_{0.3}Sn_{0.2}O_2$ (d) $NaNi_{0.5}Mn_{0.2}Sn_{0.3}O_2$ (e) $NaNi_{0.5}Mn_{0.1}Sn_{0.4}O_2$ (f) $NaNi_{0.5}Sn_{0.5}O_2$; black, red and blue lines indicate the experimental, calculated XRD patterns and the difference respectively. Bragg reflections are shown by green bar lines; Peaks due to Be window are not shown for clarity reasons. The peaks marked with asterisks (*) are

due to NiO impurity. The phases with y= 0 and 0.3-0.5 are refined with single phase and the unit cell values with atomic coordinates are given in the supplementary table ST1. The patterns with y=0.1 and 0.2 are refined with two phases having rhombohedral structure (space group: *R* -3*m*) with different unit cell parameters. The unit cells used for the refinement of $NaNi_{0.5}Mn_{0.4}Sn_{0.1}O_2$ are *a*=*b*= 3.0055, *c*= 15.9737 Å; *a*=*b*= 2.967, *c*= 15.935 Å and that of $NaNi_{0.5}Mn_{0.3}Sn_{0.2}O_2$ are *a*=*b*= 3.0448, *c*= 16.0045 Å; *a*=*b*= 3.0076; *c*= 15.99 Å respectively.

3. Supporting information S-3

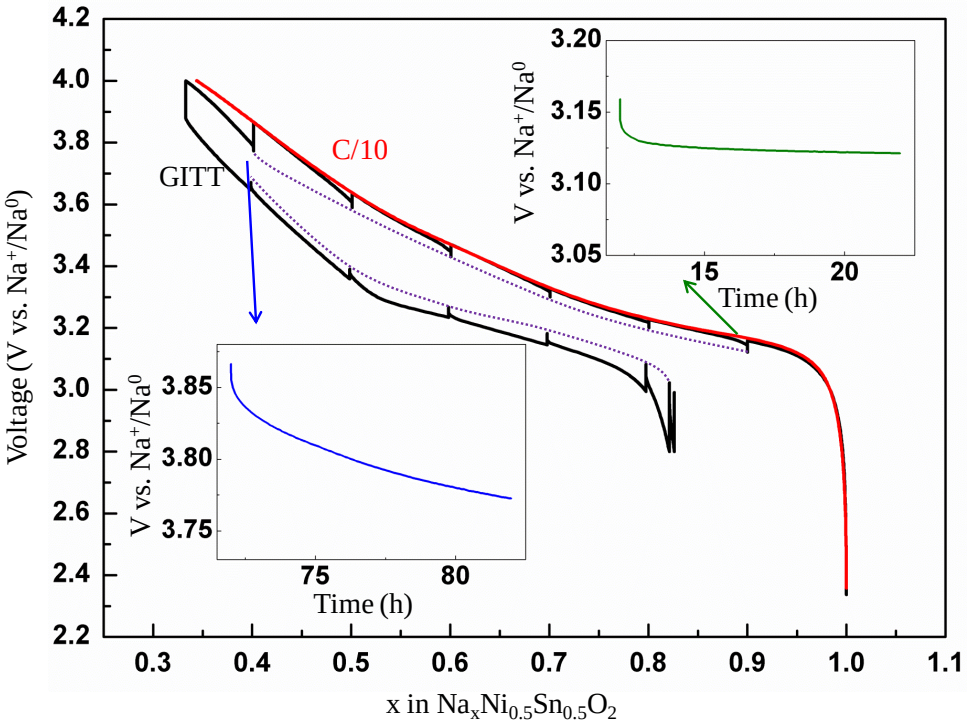

Figure. S3: GITT voltage profile (2 h, C/20 pulse, 10 h rest) of $NaNi_{0.5}Sn_{0.5}O_2$ vs. Na half cell (Black line) in comparison with the first charge profile of the cell cycled at C/10 rate (red line). The dotted lines in the plot are guide to eye to show the equilibrium potential obtained after 10h of rest. An average redox potential of 3.2 V is observed from the GITT cycling profile. The inset shows the OCV vs. Time plot at the initial stage (top) and end (bottom) of charge. Phase equilibration was observed within few minutes at the initial stages of cycling, whereas the potential reduces much faster and phase equilibrium was not reached nearing the end of charge process (near 4 V) indicating a possible side reaction with the electrolyte.

4. Supporting Information S-4

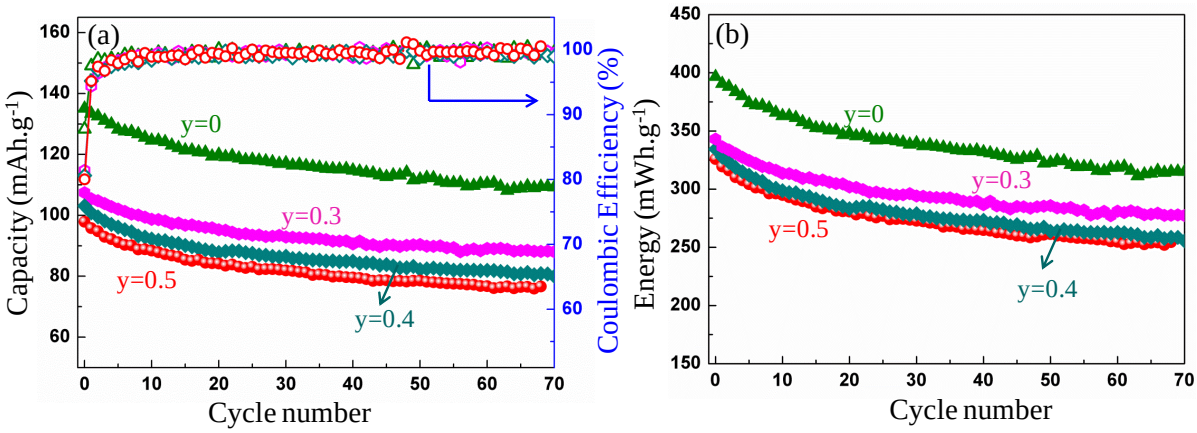

Figure. S4: (a) Capacity and (b) energy density of $NaNi_{0.5}Mn_{0.5-y}Sn_yO_2$ materials in sodium half cells cycled at C/10 rate and plotted as a function of cycle number. The first cycle coulombic efficiency of ~80 and 90 % was obtained with Sn substituted and un-substituted materials respectively (a). On subsequent cycles, the coulombic efficiency increases to > 99% for all materials (y= 0, 0.3-0.5).

5. Supporting information S-5

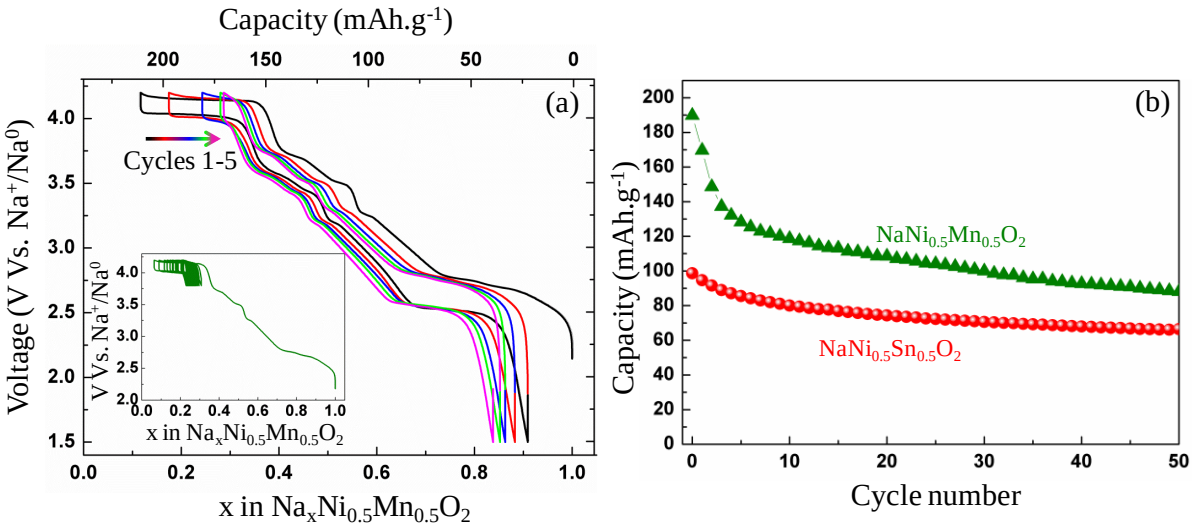

Figure. S5: (a) Galvanostatic charge- discharge profile of $NaNi_{0.5}Mn_{0.5}O_2$ in the extended voltage window of 1.5- 4.2 V. The plateau at 4.2 V degrades with continuous cycling and disappears completely after 5 cycles. Inset is the cycling profile of $NaNi_{0.5}Mn_{0.5}O_2$ vs. sodium cell cycled in the voltage window of 3.8- 4.2 V to show the deteriorating nature of 4.2 V redox process on cycling. (b) Capacity retention plot of $NaNi_{0.5}Mn_{0.5}O_2$ cycled in the voltage window of 4.2 – 2.2 V in comparison to that of $NaNi_{0.5}Sn_{0.5}O_2$ cycled between 4.2- 2.8 V. $NaNi_{0.5}Mn_{0.5}O_2$ shows much higher initial discharge capacity of ~190 mAh.g-1, however the capacity degrades much faster due to the deteriorating 4.2 V redox process.

6. Supporting information S-6

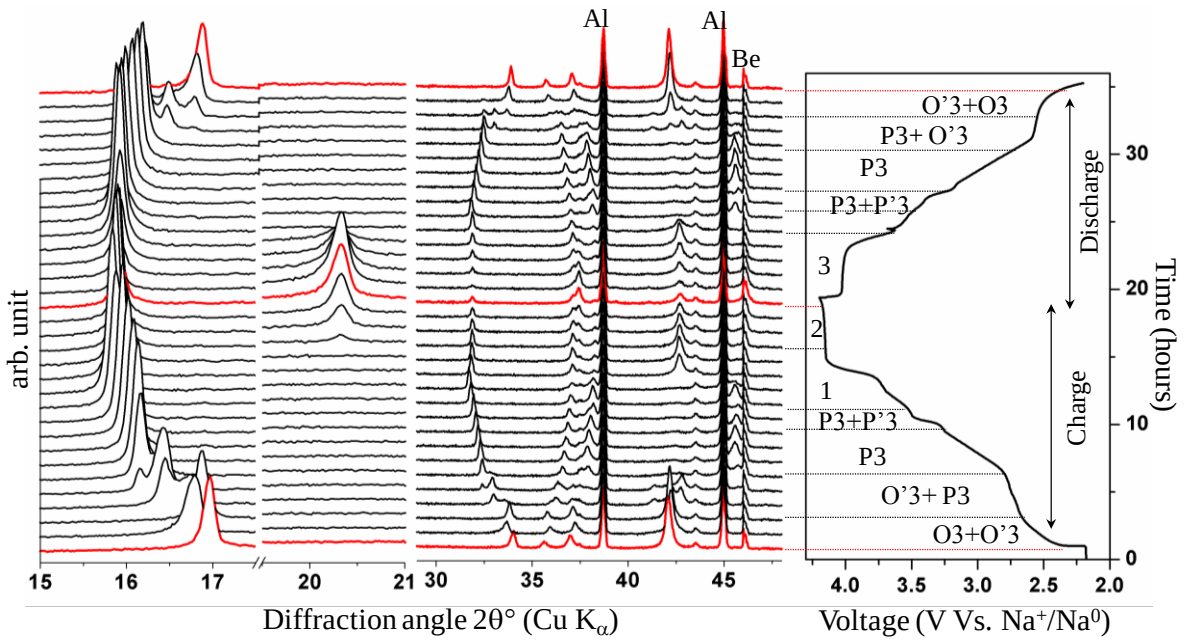

Figure. S6: *In-situ* XRD patterns of the $NaNi_{0.5}Mn_{0.5}O_2$ material on cycling the cell versus sodium metal at C/20 rate (1 sodium removal in 20 hours). The XRD pattern shows continuous evolution of phases from O3 ⇔ O'3 ⇔ P3 ⇔ P'3 etc. New biphasic regions were observed at 4.2 V (marked 1 and 2) with a new XRD peak at high angle (20.4°) indicating the phase formed has very small lattice. The change in lattice parameter as a function of sodium stoichiometry (x in $Na_xNi_{0.5}Mn_{0.5}O_2$) were derived by refining the XRD patterns with the rhombohedral (space group: *R* -3*m*) and monoclinic (*C*2/*m*) symmetries for the undistorted (O3 and P3) and monoclinically distorted (O'3, P'3) phases respectively. The derived lattice parameters are plotted in Fig. 4 of the main manuscript.

7. Supporting information S-7

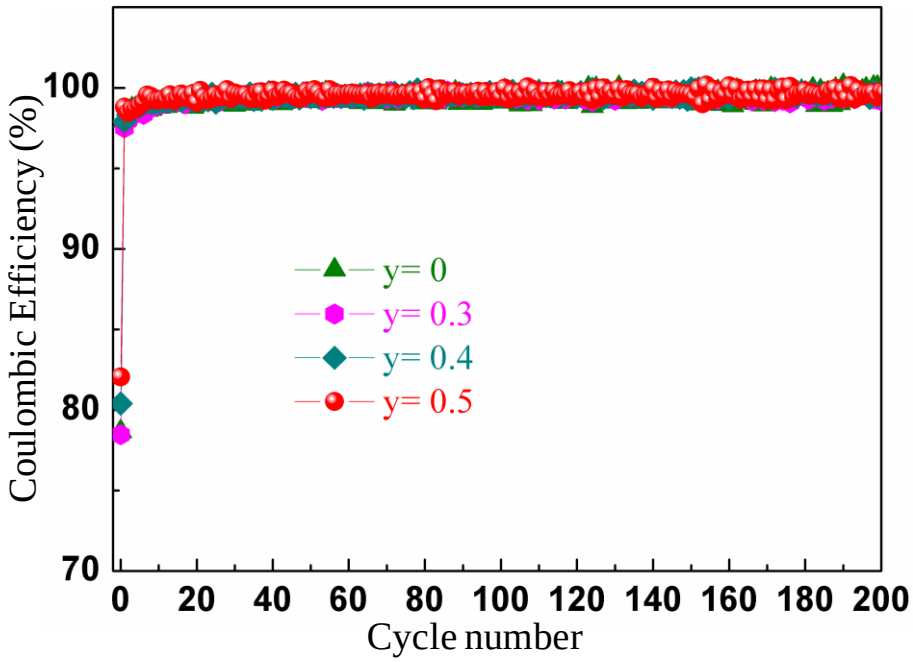

Figure. S7. Percentage coulombic efficiency of the O3 $NaNi_{0.5}Mn_{0.5-y}Sn_yO_2$ with y= 0, 0.3, 0.4 and 0.5 in sodium ion full cells. The data is derived from the full cells shown in Fig.6 of the main paper. All cells show the first cycle coulombic efficiency of ~80% which increases to > 99.8% on subsequent cycles and remains the same until 200 cycles. The low coulombic efficiency in the initial cycles is due to the irreversibility associated with the formation of solid-electrolyte interface in the hard carbon negative electrode.

8. **Supporting information S-8**

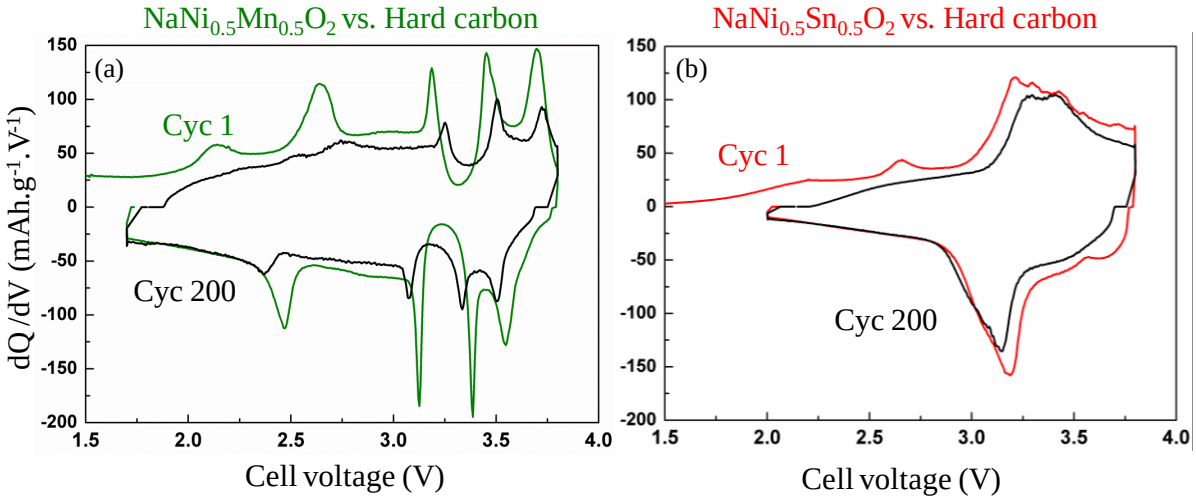

Figure. S8. Derivative plots of the (a) $NaNi_{0.5}Mn_{0.5}O_2$ and (b) $NaNi_{0.5}Sn_{0.5}O_2$ full cells for the first and 200th cycles. The amplitude of the various phase transitions observed in the first cycle of the $NaNi_{0.5}Mn_{0.5}O_2$ vs. and carbon cell reduced after 150 cycles. This explains the observed capacity decay with these materials shown in Fig. 6 of main paper. Whereas, $NaNi_{0.5}Sn_{0.5}O_2$ due to the suppressed phase transitions maintain the capacity for long cycling.

9. **(a) Supporting information S-9**: Redox potential determination

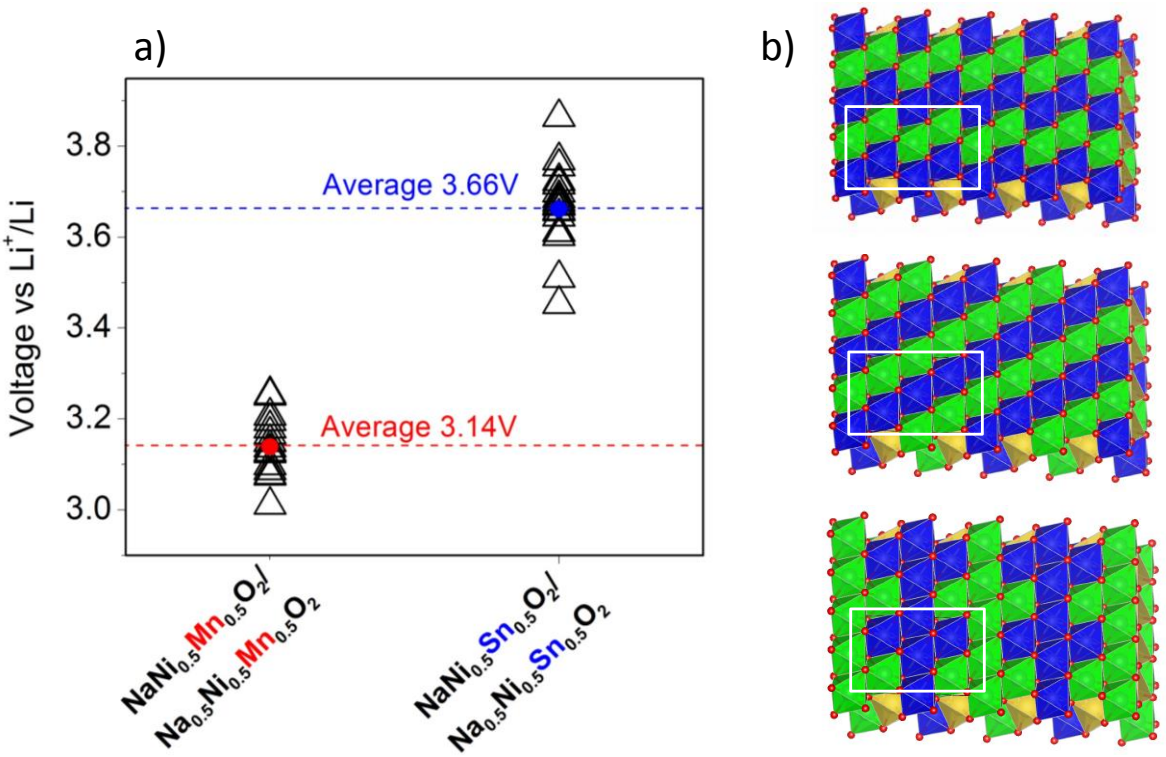

Figure. S9: a) Average cell voltages computed within the DFT+U formalism for $NaNi_{0.5}M_{0.5}O_2$ with M = Mn or Sn. Three different cation orderings are considered for the O3-type and P3-type structures in the sodiated and de-sodiated forms. Overall the potential of 18 redox couples are calculated. U values for Ni^{2+}, Ni^{3+} and Mn^{4+} are taken equal to 6 eV, 6 eV and 5 eV respectively. Calculated potentials are much higher than the experimental ones due to the imposed cation ordering and non-optimized U values, however a higher redox potential is always observed with $NaNi_{0.5}Sn_{0.5}O_2$ in comparison to $NaNi_{0.5}Mn_{0.5}O_2$. b) Three different O3 structural models with different cation ordering used for the calculations. White square is the unit cell. The P3 structural models with the same cation ordering are used for the calculations.

9. (b) Supporting information S-9: Interaction energy determination.

Total energy, E, is assumed to be expressed as a sum of interaction energies between next-nearest neighbor ions:

$$E = E_{NaNiSnO} + \sum E_{M-M} + \sum E_{M-Na} + \sum E_{Na-Na} + \sum E_{M-O} + \sum E_{Na-O} + \sum E_{O-O}$$

E_{i-j} being the interaction energies for the $i-j$ bonds. $E_{NaNiSnO}$ is an energy term for the atoms themselves. Considering energy difference between structures having the same anionic lattice, composition and M ordering but different Na ordering cancels out $E_{NaNiSnO}$, E_{M-M}, E_{M-O}, E_{Na-O} and E_{O-O} terms, so that ΔE will depend on E_{M-Na} and E_{Na-Na}.

E_{M-Na} and E_{Na-Na} will be expressed with specific interaction energies, considered to be the most important in the P3 structure: E_M and $E_{MM'M''}$ for Na sharing face with M and edge with M, M' and M'' respectively and E_{Na3} and $E_{Na3.5}$ for Na – Na distance of 3 Å or 3.5 Å.

$$\Delta E = \sum E_M + \sum E_{MM'M''} + \sum E_{Na3} + \sum E_{Na3.5}$$

At this point, choosing wisely the Na position, one can easily extrapolate interaction energies to DFT energy difference calculations. We have been interested by the $E_{Na3.5} - E_{Na3}$, and $(E_{Ni} + E_{NiNiSn}) - (E_{Sn} + E_{NiSnSn})$

These energies have been estimated with 10 different structures having different M and Na orderings.

10. Supporting information S-10

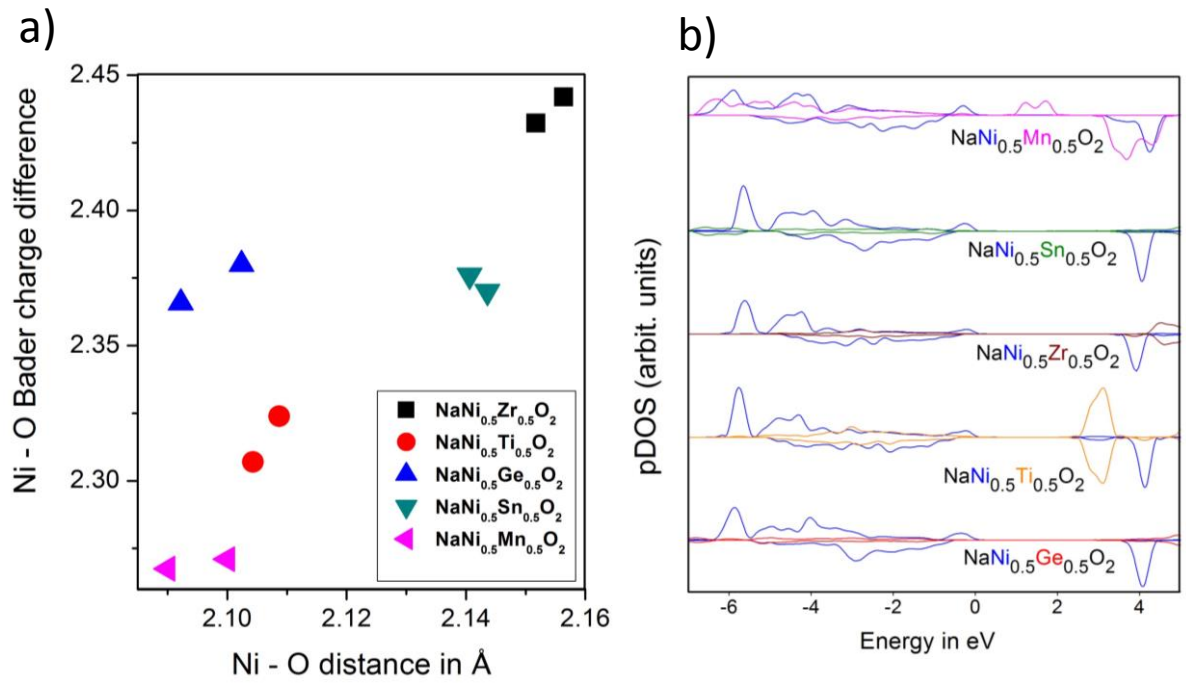

Figure. S10: a) Difference between Ni and O Bader charges calculated from DFT using two structural model with different cation orderings, presented Fig.S9(b), for $NaNi_{0.5}Zr_{0.5}O_2$, $NaNi_{0.5}Ti_{0.5}O_2$; $NaNi_{0.5}Ge_{0.5}O_2$; $NaNi_{0.5}Sn_{0.5}O_2$ and $NaNi_{0.5}Mn_{0.5}O_2$, in black, red, blue, green and magenta respectively. b) Ni and M atom-projected density of states calculated with the structural models presented Fig.S9(b) for M = Mn, Sn, Zr, Ti and Ge from top to bottom in pink, green, brown, orange and red respectively. The pDOS in (b) show no overlap between Ni and M states M = Sn, Zr, Ge implying electron localization for both d^0 and d^{10} systems with the exception of Ti^{4+} having electron delocalization closer to the Mn^{4+} due to the orbital overlap. This observation is concomitant with the Bader charge analysis that shows relatively lower Ni-O bond ionicity for $NaNi_{0.5}Ti_{0.5}O_2$ in comparison to the $NaNi_{0.5}Sn_{0.5}O_2$.

11. Supporting Information S-11

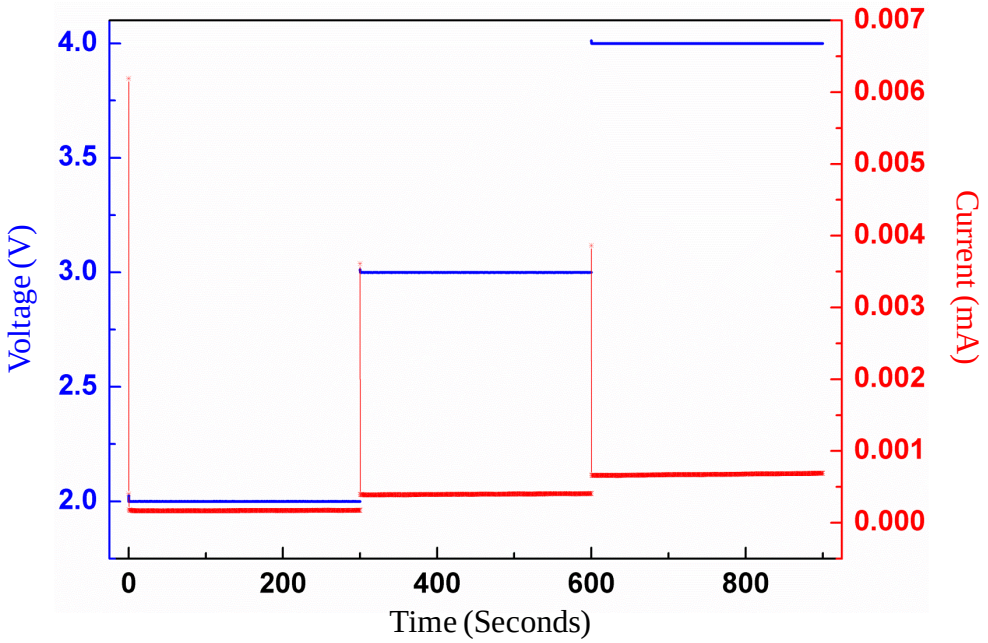

Figure. S11: Current response of $NaNi_{0.5}Sn_{0.5}O_2$ pellet for the applied potentials of 2, 3 and 4 V.

Chronoamperometric experiments were carried out in order to calculate the electronic conductivity of the $NaNi_{0.5}Sn_{0.5}O_2$. The measurements were carried out on a dense pellet of 8mm dia and 1.2 mm thickness. The pellets were sintered at 900 °C for 12 hours in argon and the measurements were done in argon atmosphere using a biologic galvanostat/potentiostat. $NaNi_{0.5}Sn_{0.5}O_2$ shows electronic conductivity of the order of 10^{-10} $S.cm^{-1}$. Such poor electronic conductivity is also visible from the color of the $NaNi_{0.5}Mn_{0.5-y}Sn_yO_2$ materials which changes from yellow to light brown, dark brown and black on moving from y= 0.5, 0.4, 0.3 and 0 respectively.

12. Supporting Information S-12

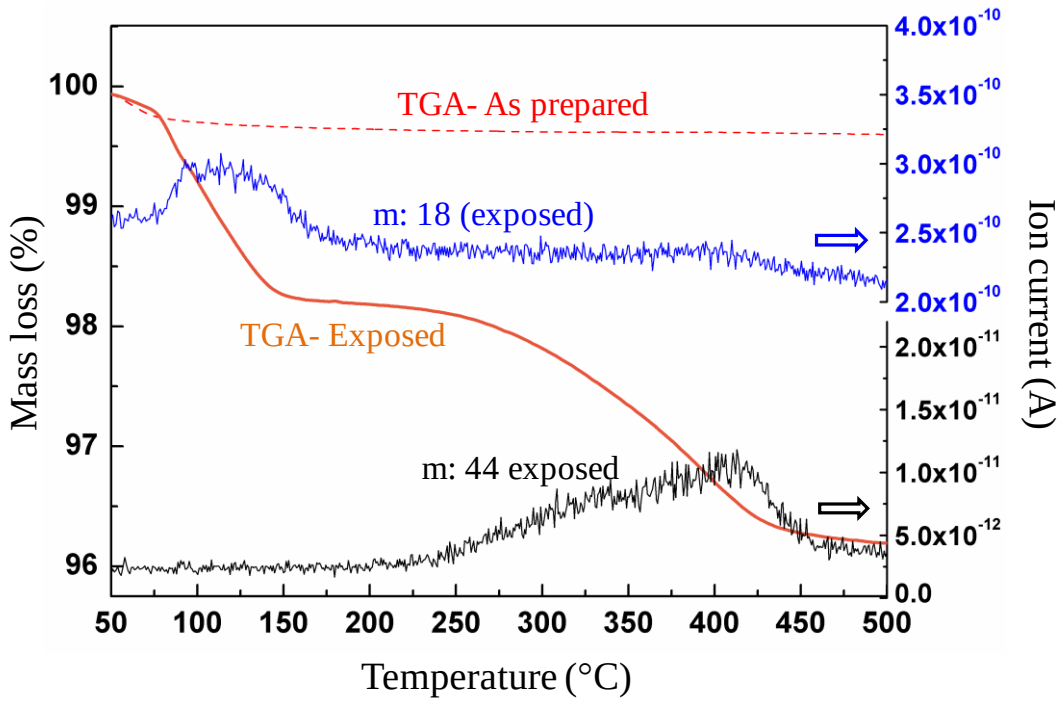

Figure. S12: Thermo gravimetric analysis data of the as prepared (red dotted line) $NaNi_{0.5}Mn_{0.5}O_2$ and the material exposed to 60% RH for 3 hours (orange solid line). The as prepared $NaNi_{0.5}Sn_{0.5}O_2$ did not show any mass loss; whereas the air exposed $NaNi_{0.5}Sn_{0.5}O_2$ showed a ~4% mass loss due to H_2O (100- 150 °C) and CO_2 (250- 450 °C). Such a CO_2 loss must be due to carbonate species in the form of Na_2CO_3 in the air exposed materials.

13. Supporting Information S13

Table ST1. Crystallographic information table obtained from the XRD Reitveld refinement data for $NaNi_{0.5}Mn_{0.5-y}Sn_yO_2$ materials with y= 0, 0.3, 0.4 and 0.5.

$NaNi_{0.5}Sn_{0.5}O_2$: *R* -3*m*, a = 3.107(5) Å; c = 16.181(1) Å; Z = 3; V/Z = 45.10(2) $Å^3$

Atom	Wyckoff position	x	y	z	Biso (Å²)	occupancy
O	*6c*	0	0	0.26517(19)	0.03(6)	1
Na	*3b*	0	0	½	1.21(6)	1
Ni	*3a*	0	0	0	0.87(2)	0.5
Sn	*3a*	0	0	0	0.87(2)	0.5

$NaNi_{0.5}Mn_{0.1}Sn_{0.4}O_2$: *R* -3*m*, a = 3.084(7) Å; c = 16.139(2) Å; Z = 3; V/Z = 44.33(3) $Å^3$

Atom	Wyckoff position	x	y	z	Biso (Å²)	occupancy
O	*6c*	0	0	0.26556(14)	0.17(5)	1
Na	*3b*	0	0	½	1.06(5)	1
Ni	*3a*	0	0	0	0.41(2)	0.5
Sn	*3a*	0	0	0	0.41(2)	0.5

$NaNi_{0.5}Mn_{0.2}Sn_{0.3}O_2$: *R* -3*m*, a = 3.059(9) Å; c = 16.088(9) Å; Z = 3; V/Z = 43.48(3) $Å^3$

Atom	Wyckoff position	x	y	z	Biso (Å²)	occupancy
O	*6c*	0	0	0.26579(9)	0.22(3)	1
Na	*3b*	0	0	½	1.19(5)	1
Ni	*3a*	0	0	0	0.44(11)	0.5
Sn	*3a*	0	0	0	0.44(11)	0.5

$NaNi_{0.5}Mn_{0.5}O_2$: *R* -3*m*, a = 2.970(3) Å; c = 15.905(5) Å; Z = 3; V/Z = 40.51(3) $Å^3$

Atom	Wyckoff position	x	y	z	Biso (Å²)	occupancy
O	*6c*	0	0	0.26784(14)	0.28(5)	1
Na	*3b*	0	0	½	1.17(5)	1
Ni	*3a*	0	0	0	0.51(2)	0.5
Sn	*3a*	0	0	0	0.51(2)	0.5